The Astrophysical Journal, 975:241 (25pp), 2024 November 10 https://doi.org/10.3847/1538-4357/ad7b31

Characterizing the Molecular Gas in Infrared Bright Galaxies with CARMA

Katherine Alatalo[1,2], Andreea O. Petric[1,2], Lauranne Lanz[3], Kate Rowlands[2,4], Vivian U[5,6], Kirsten L. Larson[4], Lee Armus[7], Loreto Barcos-Muñoz[8,9], Aaron S. Evans[8,9], Jin Koda[10], Yuanze Luo[2], Anne M. Medling[11], Kristina E. Nyland[12], Justin A. Otter[2], Pallavi Patil[2], Fernando Peñaloza[13], Diane Salim[14], David B. Sanders[15], Elizaveta Sazonova[16], Maya Skarbinski[2], Yiqing Song[17,18], Ezequiel Treister[13], and C. Meg Urry[19,20]

[1] Space Telescope Science Institute, 3700 San Martin Drive, Baltimore, MD 21218, USA; kalatalo@stsci.edu
[2] William H. Miller III Department of Physics and Astronomy, Johns Hopkins University, Baltimore, MD 21218, USA
[3] The College of New Jersey, 2000 Pennington Road, Ewing, NJ 08628, USA
[4] AURA for ESA, Space Telescope Science Institute, 3700 San Martin Drive, Baltimore, MD, USA
[5] Department of Physics and Astronomy, 900 University Avenue, University of California, Riverside CA 92521, USA[21]
[6] Department of Physics and Astronomy, 4129 Frederick Reines Hall, University of California, Irvine, CA 92697, USA
[7] Infrared Processing and Analysis Center, California Institute of Technology, 1200 East California Boulevard, Pasadena, CA 91125, USA
[8] National Radio Astronomy Observatory, 520 Edgemont Road, Charlottesville, VA 22903, USA
[9] Department of Astronomy, University of Virginia, 530 McCormick Road, Charlottesville, VA 22903, USA
[10] Dept. of Physics and Astronomy, Stony Brook University, Stony Brook, NY 11794-3800, USA
[11] Ritter Astrophysical Research Center and Department of Physics & Astronomy, University of Toledo, Toledo, OH 43606, USA
[12] U.S. Naval Research Laboratory, 4555 Overlook Avenue Southwest, Washington, DC 20375, USA
[13] Instituto de Astrofísica, Facultad de Física, Pontificia Universidad Católica de Chile, Campus San Joaquín, Avenida Vicuña Mackenna 3 4860, Macul Santiago, 7820436, Chile
[14] Physics & Astronomy, Rutgers, The State University of New Jersey, 136 Frelinghuysen Road, Piscataway, NJ 08854-8019, USA
[15] Institute for Astronomy, 2680 Woodlawn Drive, Honolulu, HI 96822, USA
[16] Department of Physics and Astronomy, University of Waterloo, 200 University Avenue West, Waterloo, Ontario, Canada N2L 3G1, Canada
[17] European Southern Observatory, Alonso de Córdova, 3107, Vitacura, Santiago, 763-0355, Chile
[18] Joint ALMA Observatory, Alonso de Córdova, 3107, Vitacura, Santiago, 763-0355, Chile[22]
[19] Yale Center for Astronomy & Astrophysics, Physics Department, P.O. Box 208120, New Haven, CT 06520, USA
[20] Department of Physics, Yale University, P.O. Box 208121, New Haven, CT 06520, USA

Received 2024 January 25; revised 2024 August 22; accepted 2024 September 11; published 2024 November 6

Abstract

We present the CO(1–0) maps of 28 infrared-bright galaxies from the Great Observatories All-Sky Luminous Infrared Galaxy Survey (GOALS) taken with the Combined Array for Research in Millimeter Astronomy (CARMA). We detect 100 GHz continuum in 16 of the 28 CARMA GOALS galaxies, which trace both active galactic nuclei (AGNs) and compact star-forming cores. The GOALS galaxies show a variety of molecular gas morphologies, though in the majority of cases the average velocity fields show a gradient consistent with rotation. We fit the full continuum spectral energy distributions (SEDs) of each of the sources using either MAGPHYS or SED3FIT (if there are signs of an AGN) to derive the total stellar mass, dust mass, and SFRs of each object. We adopt a value determined from luminous and ultraluminous infrared galaxies (LIRGs and ULIRGs) of $\alpha_{\rm CO} = 1.5^{+1.3}_{-0.8}\,M_\odot\,({\rm K\,km\,s^{-1}\,pc^2})^{-1}$, which leads to more physical values for $f_{\rm mol}$ and the gas-to-dust ratio. Mergers tend to have the highest gas-to-dust ratios. We assume the cospatiality of the molecular gas and star formation and plot the CARMA GOALS sample on the Schmidt–Kennicutt relation, where we find that they preferentially lie above the line set by normal star-forming galaxies. This hyper-efficiency is likely due to the increased turbulence in these systems, which decreases the freefall time compared to star-forming galaxies, leading to "enhanced" star formation efficiency. Line wings are present in a non-negligible subsample (11/28) of the CARMA GOALS sources and are likely due to outflows driven by AGNs or star formation, gas inflows, or additional decoupled gas components.

Unified Astronomy Thesaurus concepts: Galaxy interactions (600); Galaxy mergers (608); Interacting galaxies (802); Molecular gas (1073); Star formation (1569)

1. Introduction

There is a bimodality seen between blue, star-forming spiral galaxies to red, quiescent early-type (lenticular and elliptical) galaxies (E. P. Hubble 1926, 1936; W. Baade 1958), with a dearth of galaxies seen with transitional (green) colors (B. M. Tinsley 1978; I. Strateva et al. 2001; I. K. Baldry et al. 2004). This suggests that galaxies must transform rapidly from blue spirals and red early-types (S. M. Faber et al. 2007).

Galaxy interactions play a crucial role in galaxy evolution, having been identified as an effective way to transform star-forming disk galaxies into quiescent ellipticals (E. Holmberg 1941; A. Toomre & J. Toomre 1972), through the loss of gas angular momentum and the growth of a bulge. These interactions are also efficient at rapidly ceasing the star formation in a galaxy through a combination of gas expulsion from the system (T. Di Matteo et al. 2005; P. F. Hopkins et al. 2008) and driving gas into the circumnuclear region, where it undergoes a starburst (J. C. Mihos & L. Hernquist 1996; P. M. Bryant & N. Z. Scoville 1999; H. He et al. 2023).

---

[21] University of California Chancellor's Postdoctoral Fellow.

[22] ESA-ALMA Fellow.

Interactions also tend to be the locations of the most prolific star formation in the local universe and have long been studied in an attempt to understand the evolution of galaxies from star-forming spirals into passive, bulge-dominated systems. In that quest, the molecular gas in these systems has been considered a linchpin to the understanding of how star formation first rises rapidly, and then ultimately ceases.

Simulations of galaxy interactions seem to show a common narrative as the merger progresses (e.g., P. F. Hopkins et al. 2008; R. Teyssier et al. 2010; F. Renaud et al. 2014; J. Fensch & F. Bournaud 2021; H. He et al. 2023). Initially, (1) the galaxies form a small group or pair, (2) there is an interaction and a first pass until ultimately (3) the galaxies coalesce and go through the starbursting infrared-bright (ULIRG) phase. Then, (4) the supermassive black hole in the center ignites and blows all of the remaining circumnuclear gas out of the system (C. Ricci et al. 2017), ending in a (5) quasar phase (in which the active galactic nucleus (AGN) is visible), which then (6) decays into a post-starburst "E+A" galaxy (A. I. Zabludoff et al. 1996; A. D. Quintero et al. 2004) and ultimately a (7) quiescent galaxy. The timescale for this transformation is ~ 1 Gyr (P. F. Hopkins et al. 2008; L. Lanz et al. 2014).

Recent observations of molecular gas in post-merger systems have called into question whether the molecular gas is truly dissipated in this way. AGN-driven molecular gas outflows have now been seen in a substantial number of infrared-bright galaxies (C. Feruglio et al. 2010; F. Combes et al. 2013; K. Sakamoto et al. 2013, 2014; C. Cicone et al. 2014; S. García-Burillo et al. 2014, 2015; Y. Luo et al. 2022), challenging whether these outflows can simultaneously be ubiquitous and dramatically transform the molecular content of these galaxies on very short ($\sim$10s of Myr) timescales. Observations of Mrk 231 by K. Alatalo (2015) suggest that the importance of the molecular outflows observed in these galaxies may have much less impact than previously thought; namely, that the majority of the molecular gas taking part in the outflow will not escape and deplete from the system, due to being below the escape velocity. This lengthened the depletion time to better match the age of stellar populations in the system (G. Canalizo & A. Stockton 2000) and is able to explain the ubiquity of these outflows.

Additionally, there is further evidence that the molecular gas in these post-merger systems is able to remain beyond star formation quenching. Transitioning galaxies have now been observed to contain non-negligible reservoirs of molecular gas (K. D. French et al. 2015; K. Rowlands et al. 2015; K. Alatalo et al. 2016), suggesting that star formation quenches post-merger, before the entirety of the molecular reservoir has been removed. It is possible that an injection of kinetic energy is able to suppress star formation sufficiently that the depletion timescale of the molecular gas is even further extended (K. Alatalo et al. 2015c, 2015a; P. Guillard et al. 2015; L. Lanz et al. 2016; D. M. Salim et al. 2020). In merging systems, turbulence may have the opposite effect (J. C. Mihos & L. Hernquist 1996; C. Federrath 2013; F. Renaud et al. 2014; D. M. Salim et al. 2015; M. Sparre & V. Springel 2016; S. Bustamante et al. 2018; M. D. Thorp et al. 2022), enhancing the star formation efficiency of the nuclear molecular gas, suggesting that the role of turbulence in these transitioning galaxies is multifaceted and complex.

Shedding light on the fate of molecular gas in merging systems requires an in-depth analysis of the processes taking place in molecular gas during all phases of a galaxy's transformation, from the time of first pass in a merger, through coalescence, to the post-starburst and quiescent phases. An ideal sample to investigate the physics of molecular gas during the ULIRG/coalescence phase of interacting galaxies is the Great Observatory All-sky LIRG Survey (GOALS; L. Armus et al. 2009).[23] GOALS is drawn from the IRAS Revised Bright Galaxy sample (D. B. Sanders et al. 2003). The galaxies in the GOALS sample represent galaxies with infrared (IR) luminosities above $10^{11}\,L_\odot$. These IR luminosities infer the presence of large quantities of dust and thus molecular gas.

Recent studies have been undertaken on merging systems and galaxy pairs, investigating the impact that the interactions have on star formation (H.-A. Pan et al. 2018) and finding that with decreased separation, $f_{\rm mol}$, $\Sigma_{\rm mol}$ and star formation rate (SFR) all increase, though star formation efficiency only increases at the closest separations. M. D. Thorp et al. (2022) was able to expand upon this work using resolved mapping of star formation and molecular gas in galaxies pairs identified by the Mapping Nearby Galaxies at APO survey (K. Bundy et al. 2015), concluding that the enhanced star formation was due to a combination of enhanced gas fraction and higher star formation efficiency, implying that interactions have an impact on star formation along many different axes. While previous studies have focused on the molecular gas properties of samples of U/LIRGs (D. Downes & P. M. Solomon 1998; Y. Gao & P. M. Solomon 2004; J. Ueda et al. 2014; T. Yamashita et al. 2017), a large-scale interferometric investigation of the GOALS galaxies, especially toward the lower end of the $L_{\rm IR}$ range, has not been completed to-date. This study brings together CO imaging data available for 28 of the GOALS sample, including 15 objects with $L_{\rm IR} \lesssim 10^{11.5}\,L_\odot$, providing new insights into the behavior of star formation in a sample distinguished by its IR luminosity, where much of the previous work has focused on the objects at the highest end of the $L_{\rm IR}$ spectrum, independent of merger configuration (or lack thereof).

The Combined Array for Research in Millimeter Astronomy (CARMA)[24] is an interferometric array of 15 radio dishes (6×10.4 m and 9×6.1 m) located in the Eastern Sierras in California (D. C.-J. Bock et al. 2006) that is well-suited for morphological studies of molecular gas in interacting galaxies. Given that these galaxies tend to contain large reservoirs of molecular gas, the combination of the high-fidelity imaging of CARMA and the strong detections allows us to trace the morphologies of the molecular gas in detail and compare these distributions with other properties of the interacting galaxies, including the SFR, the degree of morphological disruptions, and the stage along the interaction life-cycle.

We present and discuss molecular gas observations of GOALS galaxies taken with CARMA. In Section 2, we describe the selection to build the CARMA GOALS sample. In Section 3, we describe how the data were reduced and how data products were created for each object. In Section 5, we derive the physical properties of the molecular gas and discuss the implications of these observations. In Section 6, we present our conclusions. The cosmological parameters $H_0 = 70\ {\rm km\,s^{-1}}$, $\Omega_{\rm m} = 0.3$, and $\Omega_\Lambda = 0.7$ (D. N. Spergel et al. 2007) are used throughout.

---

[23] http://goals.ipac.caltech.edu/

[24] http://www.mmarray.org

Table 1
CARMA GOALS Properties and Observing Parameters

Object Name (1)	R.A. J2000 (2)	Decl. J2000 (3)	z (4)	D (Mpc) (5)	Morph. Class (6)	$\log(L_{\mathrm{IR}})$ ($L_\odot$) (7)	Semester (8)	Total (hr) (9)	Gain Cal (10)	Beam $'' \times ''$ (11)	KperJy (12)
MCG+12-02-001	00:54:03.6	+73:05:12	0.01570	68.1	m	11.4	2010a	5.0	0217+738	5.05 × 4.01	4.55
CGCG 436-030	01:20:02.7	+14:21:43	0.03123	137.0	m	11.6	2010b	4.9	0108+015	1.88 × 1.67	29.24
III Zw 35	01:44:30.5	+17:06:05	0.02740	119.8	em	11.6	2008b	4.5	0238+166	4.08 × 3.37	6.71
NGC 695	01:51:14.2	+22:34:57	0.03247	142.5	nm	11.6	2010a	2.4	0205+322	4.67 × 3.37	5.85
NGC 958	02:30:42.8	-02:56:20	0.01914	83.2	nm	11.2	2010b	12.5	0239-025	3.11 × 2.96	10.00
UGC 02369	02:54:01.8	+14:58:25	0.03120	136.8	em	11.6	2008b	2.0	0238+166	4.20 × 3.19	6.87
UGC 02608	03:15:01.4	+42:02:09	0.02334	101.8	nm	11.4	2010b	3.7	3C84	2.86 × 2.46	13.06
IRAS 03582+6012	04:02:32.5	+60:20:40	0.03001	131.5	m	11.4	2010b	8.7	0359+509	2.97 × 2.38	13.03
NGC 1614	04:33:59.8	-08:34:44	0.01594	69.1	m	11.6	2012b	8.9	0423-013	3.21 × 2.93	9.81
CGCG 468-002	05:08:20.4	+17:21:59	0.01819	79.0	em	11.1	2011a	10.3	0530+135	3.10 × 2.74	10.86
NGC 2146	06:18:37.7	+78:21:25	0.00298	12.8	m	11.1	2010b	5.6	0841+708	3.26 × 2.94	9.61
NGC 2623	08:38:24.1	+25:45:17	0.01851	80.4	m	11.5	2012a	5.9	0854+201	2.94 × 2.39	13.12
Arp 55	09:15:55.1	+44:19:55	0.03930	173.4	m	11.7	2012a	7.5	0920+446	4.37 × 3.43	6.15
UGC 05101	09:35:51.6	+61:21:11	0.03937	173.7	m	12.0	2012b	4.9	0958+655	1.76 × 1.44	36.26
Arp 148	11:03:53.6	+40:50:57	0.03452	151.7	m	11.6	2008b	3.2	0927+390	3.74 × 3.34	7.89
Arp 299	11:28:32.3	+58:33:45	0.01030	44.5	m	11.9	2013a, 14a	7.4	1153+495	2.33 × 2.25	17.58
NGC 4418	12:26:54.6	-00:52:39	0.00726	31.3	nm	11.1	2011a	6.5	3C273	0.83 × 0.70	159.00
NGC 4922	13:01:24.9	+29:18:46	0.02359	102.9	m	11.3	2010b	4.8	1310+323	2.00 × 1.31	35.16
IC 860	13:15:03.5	+24:37:08	0.01116	48.2	nm	11.2	2012a, 14a	5.0	1310+323	2.29 × 1.29	32.00
VV 250	13:15:32.8	+62:07:37	0.03083	135.2	m	11.7	2010a	13.9	0958+655	4.46 × 3.63	5.69
NGC 5256	13:38:17.5	+48:16:37	0.02786	121.9	m	11.5	2010a	4.1	1310+323	3.86 × 3.33	7.16
CGCG 142-034	18:16:40.6	+22:06:46	0.01868	81.2	m	11.1	2011a	12.1	1751+096	2.44 × 1.86	20.32
NGC 6670	18:33:35.4	+59:53:20	0.02885	126.3	m	11.6	2008b	5.5	1642+689	1.50 × 0.95	65.05
NGC 6786	19:10:53.9	+73:24:37	0.02502	109.2	m	11.4	2008b	10.1	1927+739	3.83 × 3.33	7.22
NGC 6926	20:33:06.1	-02:01:39	0.01961	85.3	m	11.3	2010b	5.5	2134-018	2.89 × 2.62	12.15
II Zw 96	20:57:23.9	+17:07:39	0.03610	158.9	m	11.9	2008b	5.5	2148+069	3.22 × 2.55	11.22
IC 5298	23:16:00.7	+25:33:24	0.02742	119.9	nm	11.5	2010a	6.9	2236+284	3.02 × 2.92	10.42
NGC 7674	23:27:56.7	+08:46:45	0.02892	126.6	em	11.5	2010b	7.3	0010+109	2.54 × 2.42	15.02

Note. Column (1): Object name. Columns (2–3): R.A./decl. of central CO pointing. Column (4): Redshift from NED. Column (5): Luminosity distance to object. Column (6): Morphological class using the classification scheme of A. O. Petric et al. (2018), of "m" for merger, "em" for early merger, and "nm" for non-merger. Column (7): Total IR luminosity from D. B. Sanders et al. (2003). Column (8): CARMA observing semester(s). Column (9): Total CARMA on-source observing hours. Column (10): The gain calibrator for observations. Column (11): The synthesized beam (in arcseconds). Column (12): The total Kelvin per Jansky factor of the observation.

2. The Sample

The sample presented in this work was drawn by cross-referencing the GOALS (L. Armus et al. 2009) sample with objects available within the CARMA archive.[25] To derive the sample presented in this paper, we ran a $\approx 1'$ proximity match for the 202 objects in GOALS (L. Armus et al. 2009), searching for all data sets that contained observations for the CO(1–0) line and requiring complete velocity coverage of the line. This overall crossmatching resulted in 31 objects. We report on 28 objects, excluding Arp 220 and NGC 6240, which are described in detail in S. Manohar & N. Scoville (2017), and Markarian 231, which is described in detail in K. Alatalo (2015). Table 1 lists the names and characteristics of the cross-matched GOALS galaxies, as well as the CARMA observing parameters, detailed below. The objects in the CARMA GOALS sample span the range of IR luminosities defined for LIRGs and ULIRGs, from $10^{11.1-12.5}\,L_\odot$. Figure 1 shows the PanSTARRS $g\,r\,i$ data (K. C. Chambers et al. 2016) of the sources represent a large swath of morphologies, from clear interactions (like II Zw 96) to semi-settled and quiescent objects (e.g., NGC 4418).

3. Observations and Analysis

3.1. CARMA Observations

CARMA observations for GOALS sources with CO(1–0) data were downloaded from the archive. Observations were taken between 2008 July and 2014 June, in a large set of array configurations and correlator configurations. The field of view of these observations corresponds to the primary beam of the 6 m antennas at 3 mm of $\approx 100''$. Data reduction was done in identical fashion to K. Alatalo et al. (2013), utilizing the Multichannel Image Reconstruction, Interactive Analysis, and Display software (MIRIAD; R. J. Sault et al. 1995). Table 1 presents the semester of observations, synthesized beam, and gain calibrators used for each CARMA GOALS object.

The available correlator configurations varied significantly from semester to semester over the 6 yr that these observations were taken. Observations taken in early semesters (e.g., III Zw 35, Arp 148) often required use of a broadband low-resolution configuration to capture the entire footprint of the CO(1–0) line. In these cases, the channel width is often 80 km s^{-1}. Despite this, all early observed galaxies have CO lines that have been resolved, with at least seven channels across them. In later semesters, the observations were taken using the upgraded correlator, which simultaneously provided

---

[25] http://carma-server.ncsa.uiuc.edu:8181/

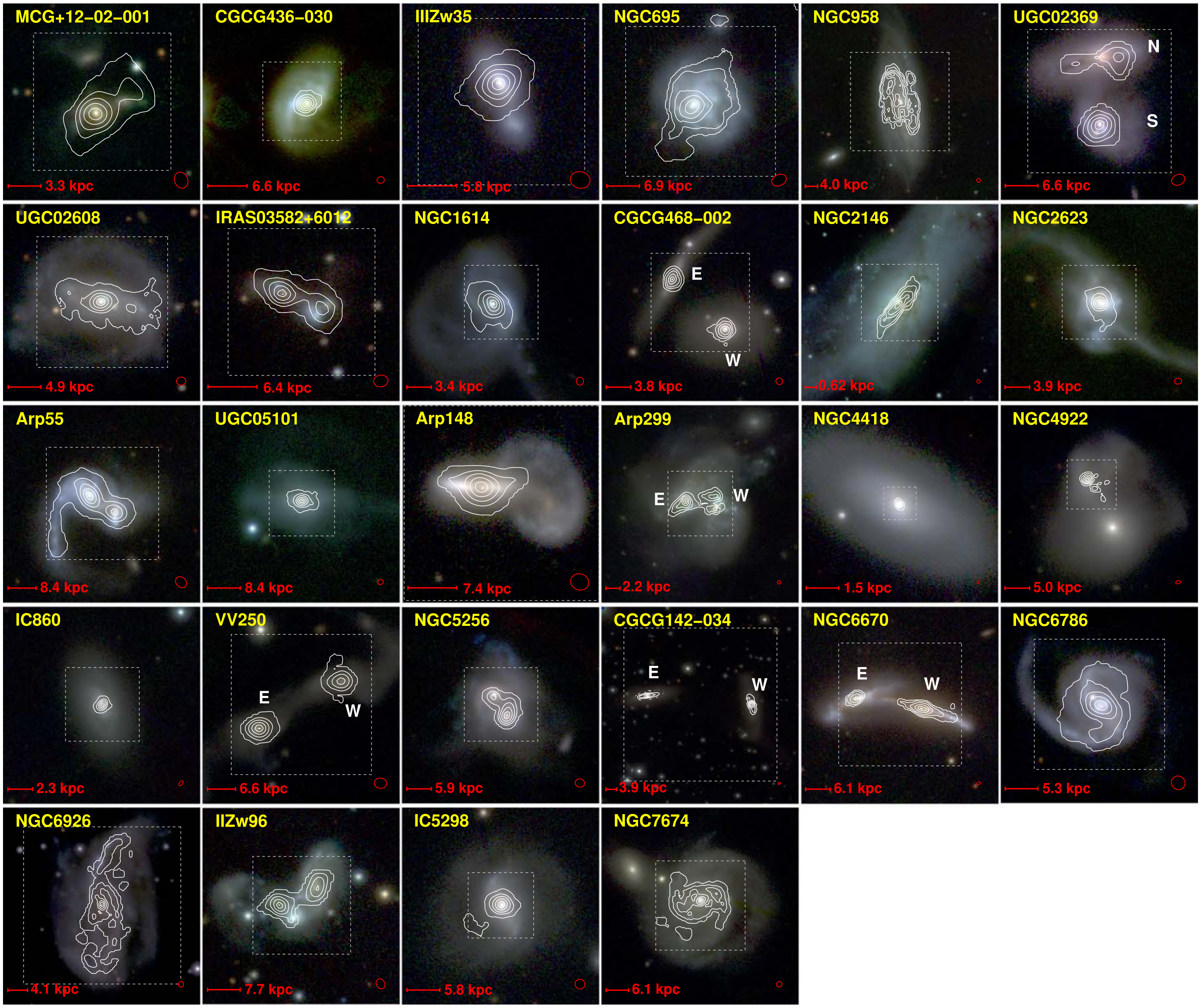

Figure 1. The CO(1–0) integrated intensity (moment0) maps from CARMA (white contours) are overlaid on the three-color *g r i* images from PanSTARRS (K. C. Chambers et al. 2016) for the 28 CARMA GOALS galaxies, ordered based on their R.A. For each map, north is up and east is to the left. The red bar in the lower left-hand corner demarcates 10″ in each field (with the corresponding physical scale listed). The beam is shown in the lower right-hand corner in red. The gray dotted borders represent the size of the CO-only moments from Figures 2 and 3.

large bandwidth and high resolution, and provided a marked improvement in resolution across the line.

3.1.1. Calibration and Imaging

The resulting moment maps were constructed in an identical fashion to K. Alatalo et al. (2013).[26] Figures 1 and 2 showcase the CARMA integrated intensity (moment0) data for each individual GOALS source, overlaid on PanSTARRS *g r i* data (K. C. Chambers et al. 2016), and on its own, respectively. Figure 3 presents the mean velocity (moment1) maps of the GOALS galaxies.

The integrated spectra are constructed by using the moment0 map to create a clip mask and integrating the flux within the moment0-defined (unmasked) aperture. This was done separately for each object. Clearly differentiable doubles, defined as those objects that could be unambiguously separated into two distinct forms in their moment0 maps, combined with confirmation of two obvious sources in the optical data, were also identified. These doubles include UGC 02369, CGCG 468-002, Arp 299, VV 250, CGCG 142-034, and NGC 6670. In these cases, the moment0 map clip mask was separated to distinguish between the gas distributions of each object. Figure 4 shows the CO(1–0) spectra integrated in this way, with the channels used to calculate the integrated line flux for each galaxy shaded in violet. For the six objects deemed to be doubles, we also show the spectra of each of the individual objects as a separate spectrum in the panel.

The root mean square (rms) per channel is calculated by (1) taking the standard deviation of all pixels within the cube that were outside the moment0 aperture, (2) applying an additional noise up-correction of 30% to account for the oversampling of the maps (see: K. Alatalo et al. 2015b for details), and (3)

---

[26] Full description available in Section 3.2

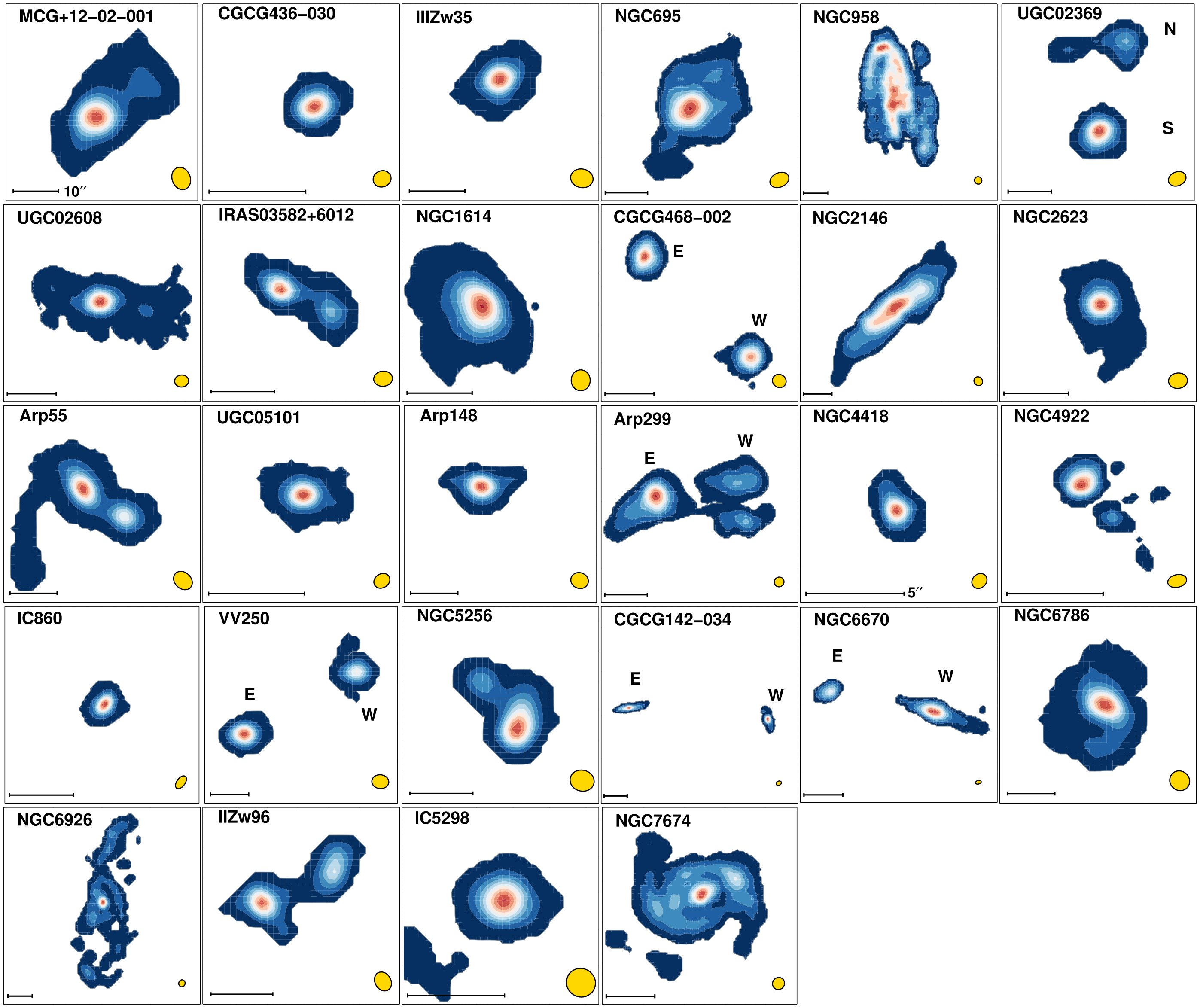

Figure 2. The CO(1–0) integrated intensity (moment0) maps of the 28 CARMA GOALS galaxies. The black bar in the lower left-hand corner demarcates 10″ in each field. The beam is shown in the lower right-hand corner in yellow, confirming that all galaxies are well-sampled.

multiplying by the square root of the total number of beams represented in the moment0 aperture.

To calculate the integrated line flux for each galaxy, we summed the shaded channels in Figure 4 and multiplied by the velocity width of each channel. The line flux rms was calculated by multiplying the rms per channel by the channel velocity width and the square root of the total number of channels containing line emission. Table 2 presents the line flux, total CO(1–0) area subtended, and other derived molecular gas properties of the CARMA GOALS sample. It is important to note that the errors quoted also do not include the 20% flux calibration uncertainties associated with CARMA observations.[27]

3.1.2. Continuum Imaging

We isolated the line-free channels using the MIRIAD task `uvlin`.[28] We then inverted the line-free visibilities using the multifrequency synthesis options with MIRIAD, creating an integrated image to search for 100 GHz continuum emission present in each of the CARMA GOALS galaxies. Of the 28 galaxies that are part of this sample, 16 contained detectable 100 GHz continuum emission. Figure 5 shows the continuum maps of these objects.

To calculate the total 100 GHz flux for each of the detected objects, we pinpointed the location of the peak in the image using the IDL routine `find_galaxy`.[29] We then created a box centered on the peak emission with twice the major axis of the beam on a side and summed all emission inside this box. The detected 100 GHz continuum emissions in these sources are centrally concentrated, and therefore it is unlikely that significant extended emission is being missed. To calculate the rms noise, we used this box to mask emission and calculated the standard deviation of the unmasked pixels with IDL routine `robust_sigma`.[30] In the cases of 100 GHz

---

[27] https://www.mmarray.org/memos/carma_memo59.pdf

[28] http://www.atnf.csiro.au/computing/software/miriad/doc/uvlin.html

[29] http://www-astro.physics.ox.ac.uk/~mxc/software/

[30] https://idlastro.gsfc.nasa.gov/ftp/pro/robust/robust_sigma.pro

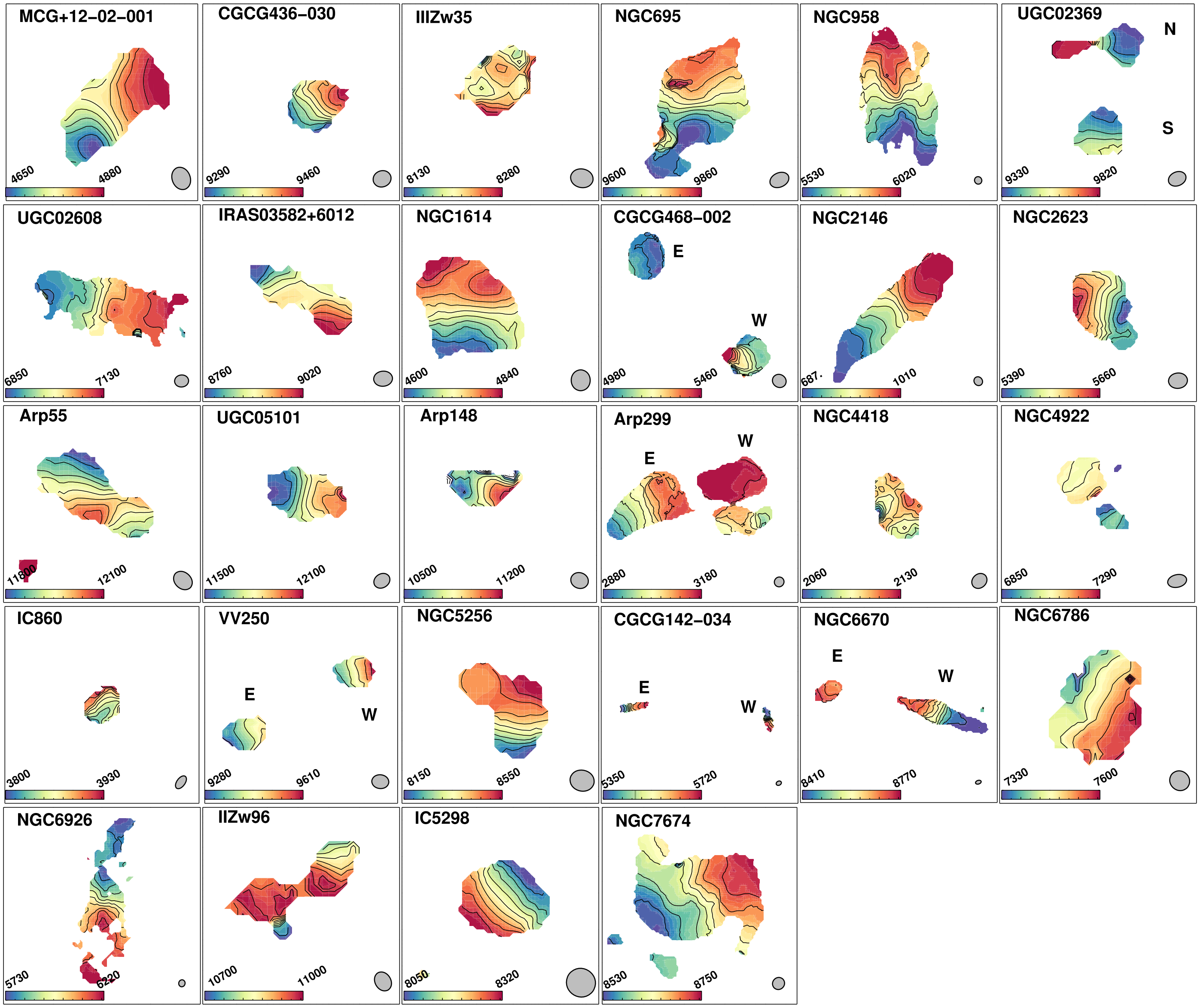

Figure 3. The mean velocity (moment1) maps of CO(1–0) of the 28 CARMA GOALS galaxies. The size scales are identical to those used in Figure 2.

nondetected sources, we calculated the 3σ upper limits in an equivalent area (twice the size of the beam major axis) to the detected sources. Table 2 lists the 100 GHz fluxes, upper limits, and rms noise.

3.2. Multiwavelength Photometry

All of the galaxies in our sample were observed with the Herschel Space Observatory (G. L. Pilbratt et al. 2010). These photometric measurements were published in J. K. Chu et al. (2017). Over half of our sample was included in the spectral energy distribution (SED) analysis of V. U et al. (2012). For these galaxies, we used the Galaxy Evolution Explorer (GALEX; D. C. Martin et al. 2005), optical (UBVRI), the 2 Micron All Sky Survey (2MASS; M. F. Skrutskie et al. 2006), and Spitzer (M. W. Werner et al. 2004) photometry from V. U et al. (2012). We applied foreground extinction corrections to the UV and optical bands, as described in the next two sections, using the Galactic extinction values from E. F. Schlafly & D. P. Finkbeiner (2011) provided in the NASA Extragalactic Database (NED). For the remaining CARMA GOALS sources detailed below, we determined the apertures for photometry based on a visual inspection of the PanSTARRS optical imaging and then applied extinction corrections. We elected to use SDSS for NGC 4922N due to anomalies in the PanSTARRS data. Tables 5, 6, and 7 present these data.

In the UV, optical, near-infrared (NIR), and mid-infrared (MIR) we convolve the catalog error in quadrature with a calibration error of 20%, 10%, 15%, and 10% of the flux, respectively, to allow for differences in the methods used to measure total photometry and errors in the spectral synthesis models used to fit the underlying stellar populations, following K. Rowlands et al. (2012). Due to the additional uncertainties in the aperture photometry of the highly blended source NGC 4922N, we convolve the catalog error with a calibration error of 20% in the optical.

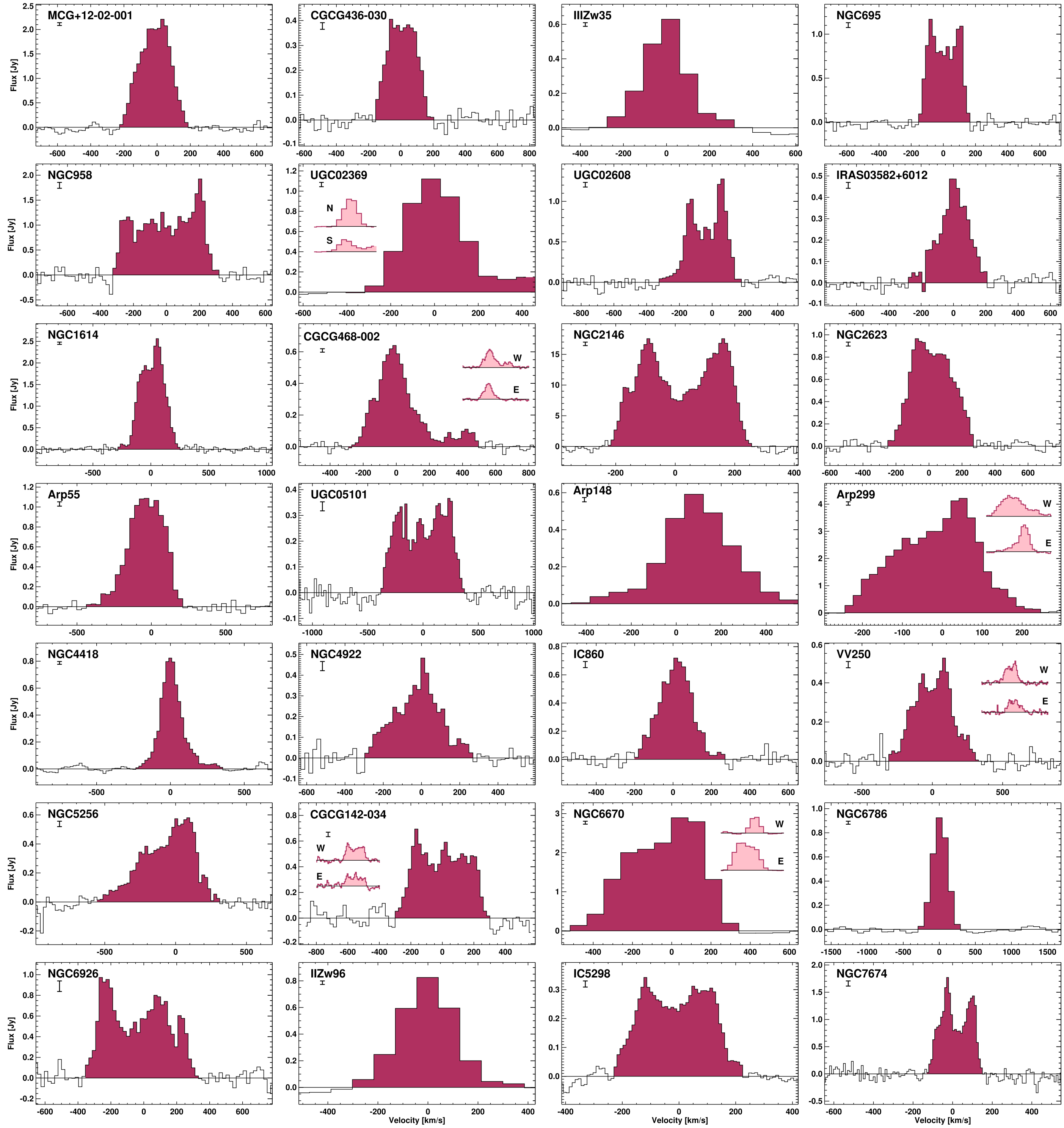

Figure 4. The integrated CO(1–0) spectra for the 28 CARMA GOALS galaxies. Each spectrum was created by using the moment0 map (shown in Figure 2) as a clip mask and totaling all flux within the mask in each channel. The areas shaded in fuchsia denote the channels used to calculate the total flux. The rms noise per channel is shown in the upper left-hand corner below the galaxy name. In all cases, the CO(1–0) is detected to be very high signal to noise. The six CARMA objects (UGC 02369, CGCG 468-002, Arp 299, VV 250, CGCG 142-034, and NGC 6670), where two different galaxies were differentiable in our data have had their spectra separated and plotted in the corner of the panel.

3.2.1. GALEX Photometry

Of the total 23 galaxies in our sample observed with GALEX, eight were not included in the set examined by J. H. Howell et al. (2010) and V. U et al. (2012). The observations for these galaxies were retrieved from the Mikulski Archive for Space Telescopes using GalexView version 1.4.11. To calculate fluxes from the background-subtracted count rate, we used the conversions provided by

Table 2
CARMA GOALS Measured Values

Name	$v_{\rm sys}$	$z_{\rm CO}$	Chan. width	Vel. range	S_{100}	$\sigma_{\rm RMS}$	$S_{\rm CO}$	Area		$L_{\rm CO}$
	(km $\rm s^{-1}$)		(km $\rm s^{-1}$)	(km $\rm s^{-1}$)	(mJy)	(mJy)	(Jy km $\rm s^{-1}$)	(sq.arcsec)	(kpc^2)	(10^4 $L_\odot$)
(1)	(2)	(3)	(4)	(5)	(6)	(7)	(8)	(9)	(10)	(11)
MCG+12-02-001	4780	0.0159	20.6	4559–4972	45.16 ± 0.48	6.61	501.8 ± 0.8	470.8	49.5	28.23 ± 0.05
CGCG 436-030	9370	0.0312	21.3	9222–9563	9.54 ± 0.37	4.60	91.6 ± 0.4	33.9	13.2	19.99 ± 0.09
III Zw 35	8230	0.0274	84.5	7993–8500	<13.35	3.65	155.0 ± 1.0	145.6	44.2	26.05 ± 0.17
NGC 695	9720	0.0324	21.3	9564–9862	<3.18	5.23	225.0 ± 0.6	499.8	209.5	52.94 ± 0.14
NGC 958	5770	0.0192	20.8	5451–6075	<0.89	5.66	610.7 ± 0.7	1289.5	196.3	50.20 ± 0.06
UGC 2369N	9430	0.0315	81.3	9071–9559	<16.24	5.28	108.9 ± 1.6	132.6	52.4	24.08 ± 0.35
UGC 2369S	9450	0.0315	81.3	9071–9559	⋯	⋯	206.2 ± 1.6	119.3	47.3	45.81 ± 0.35
UGC 02608	7040	0.0235	20.9	6725–7207	6.02 ± 0.18	4.53	253.5 ± 0.6	357.7	80.3	31.11 ± 0.07
IRAS 03582+6012	8900	0.0297	21.2	8634–9100	0.86 ± 0.18	3.61	99.8 ± 0.4	133.0	47.1	19.66 ± 0.08
NGC 1614	4730	0.0158	20.6	4456–4972	25.76 ± 0.34	5.52	603.1 ± 0.6	275.8	28.5	33.29 ± 0.03
CGCG 468-002W	5030	0.0168	20.7	4766–5510	2.77 ± 0.20	2.88	60.2 ± 0.4	65.6	7.6	3.76 ± 0.02
CGCG 468-002E	5140	0.0171	20.7	4869–5614	3.58 ± 0.20	⋯	102.6 ± 0.4	68.0	8.3	6.69 ± 0.02
NGC 2146	874.	0.0029	10.1	653–1136	<12.43	35.1	4913. ± 3.1	776.0	2.8	9.19 ± 0.01
NGC 2623	5510	0.0184	20.8	5275–5773	43.97 ± 0.35	4.41	295.3 ± 0.5	143.3	20.0	22.18 ± 0.04
Arp 55	11960	0.0399	32.4	11544–12160	5.47 ± 0.25	4.64	338.8 ± 0.7	422.5	263.4	121.19 ± 0.26
UGC 05101	11780	0.0393	21.6	11412–12147	24.35 ± 0.41	4.49	174.5 ± 0.6	49.9	30.2	60.52 ± 0.21
Arp 148	10350	0.0345	84.1	10014–10939	<185.1	4.14	211.9 ± 1.3	123.9	58.6	56.56 ± 0.34
Arp 299W	3080	0.0103	20.4	2827–3337	48.62 ± 0.53	7.56	587.2 ± 0.9	203.6	9.0	13.68 ± 0.02
Arp 299E	3170	0.0106	20.4	2908–3419	17.99 ± 0.53	⋯	346.8 ± 0.9	239.5	11.2	8.55 ± 0.02
NGC 4418	2100	0.0070	20.3	1878–2446	0.84 ± 0.16	3.25	141.1 ± 0.4	7.5	0.1	1.53 ± 0.01
NGC 4922	7080	0.0236	21.0	6797–7342	<1.42	6.58	108.4 ± 0.7	38.2	8.7	13.48 ± 0.09
IC 860	3880	0.0129	20.5	3684–4136	30.86 ± 0.57	7.11	145.7 ± 0.7	35.3	2.5	5.39 ± 0.03
VV250W	9420	0.0314	21.3	9129–9725	3.90 ± 0.31	4.76	58.7 ± 0.6	118.4	46.7	12.96 ± 0.13
VV250E	9400	0.0314	21.3	9108–9704	6.63 ± 0.31	⋯	93.4 ± 0.6	105.6	41.5	20.55 ± 0.14
NGC 5256	8460	0.0282	21.1	7916–8762	15.74 ± 0.41	5.74	230.9 ± 0.8	167.1	53.6	41.05 ± 0.15
CGCG 142-034W	5540	0.0185	20.8	4881–5793	<1.03	3.70	228.9 ± 0.6	113.6	16.0	17.37 ± 0.04
CGCG 142-034E	5470	0.0182	20.7	4757–5709	⋯	⋯	93.3 ± 0.6	172.7	23.7	6.90 ± 0.04
NGC 6670W	8540	0.0285	81.3	8033–8846	<21.07	4.27	984.0 ± 1.2	105.1	34.3	178.37 ± 0.22
NGC 6670E	8720	0.0291	81.3	8196–9008	⋯	⋯	248.6 ± 1.3	32.1	10.9	46.97 ± 0.24
NGC 6786	7500	0.0250	84.1	7244–7748	<6.28	2.86	245.1 ± 0.7	422.8	107.3	34.16 ± 0.10
NGC 6926	6040	0.0201	20.8	5695–6361	<0.94	5.42	364.8 ± 0.7	870.0	145.0	32.91 ± 0.06
II Zw 96	10920	0.0364	85.9	10662–11264	<23.10	3.41	222.7 ± 1.1	153.0	80.2	66.26 ± 0.33
IC 5298	8200	0.0274	10.6	7980–8423	3.57 ± 0.30	3.64	95.9 ± 0.3	96.7	29.2	16.03 ± 0.05
NGC 7674	8630	0.0288	10.0	8507–8778	11.64 ± 0.47	5.96	252.3 ± 0.4	496.7	165.6	46.71 ± 0.07

Note. Column (1): Object name. Column (2): Systemic velocity of the CO emission in km $\rm s^{-1}$, defined as the center of the CO emission. Column (3): Redshift derived from the CO. Column (4): Channel width in km $\rm s^{-1}$. Column (5): Velocity range of detected CO emission in km $\rm s^{-1}$. Column (6): 100 GHz continuum emission in mJy. Column (7): Rms noise per channel in mJy $\rm beam^{-1}$. Column (8): CO(1–0) flux in Jy km $\rm s^{-1}$ Columns (9–10): The total area subtended by the CO, in celestial (sq.arcsec) and physical (kpc^2) units. Column (11): The total CO luminosity in 10^4 $L_\odot$.

G. S. F. Center (2004):[31]

$$f_{\rm NUV} = 2.06\times10^{-16}\times ct_{\rm NUV} \quad \text{and}$$
$$f_{\rm FUV} = 1.40\times10^{-15}\times ct_{\rm FUV},$$

where $ct_{\rm NUV}$ and $ct_{\rm FUV}$ are background corrected count rates and the fluxes are given in erg $\rm s^{-1}\,cm^{-2}\,\AA^{-1}$. The background rate is estimated in a source-free region near each galaxy. We also masked out foreground and background objects within the source aperture. The observed UV fluxes are corrected for foreground Galactic extinction using the relations given by T. K. Wyder et al. (2005), where $E(B-V)$ is calculated from the E. F. Schlafly & D. P. Finkbeiner (2011) A_V assuming an $R_V = 3.1$ reddening law (E. L. Fitzpatrick 1999):

$$A_{\rm NUV} = 8.376\times E(B-V) \text{ and}$$
$$A_{\rm FUV} = 8.741\times E(B-V).$$

Photometric uncertainties consist of the 10% calibration uncertainty (G. S. F. Center 2004) combined in quadrature with Poisson uncertainty.

3.2.2. PanSTARRS photometry

Calibrated PanSTARRS cutout images in the g, r, and i bands were downloaded from the archive.[32] Per PanSTARRS documentation,[33] the CD matrices in the FITS headers of these files were first updated with the IDL routine `FITS_CD_FIX`. Given the photometric zero-point of $25 + 2.5\ \log(t_{\rm exp})$ (D. Jones 2024, private communication) and standard $f_0 = 3631$ Jy (J. B. Oke & J. E. Gunn 1983), we obtained the fluxes in Jy via the following:

$$m_{g,r,i} = -2.5\log(ct_{g,r,i}) + 2.5\log(t_{\rm exp}) + 25,$$
$$f_{g,r,i} = 3631\times10^{\frac{m_{g,r,i}}{-2.5}},$$

---

[31] https://asd.gsfc.nasa.gov/archive/galex/FAQ/counts_background.html

[32] http://ps1images.stsci.edu/cgi-bin/ps1cutouts

[33] https://outerspace.stsci.edu/display/PANSTARRS/

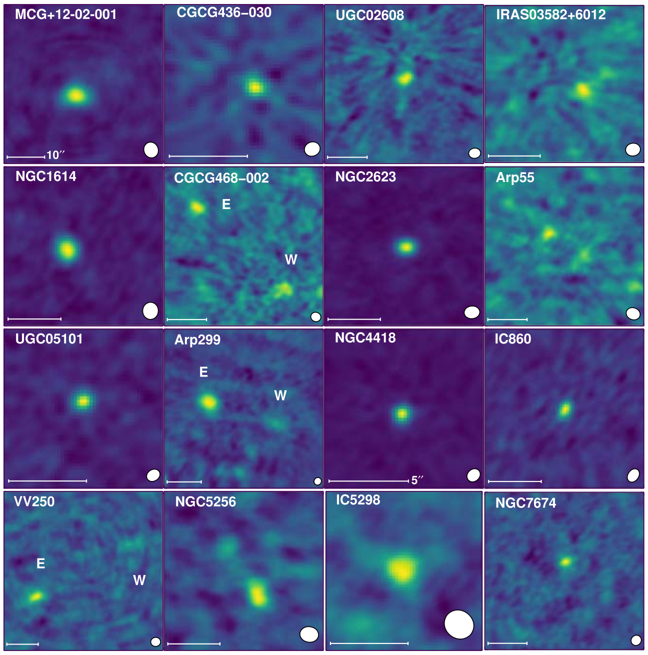

Figure 5. The 100 GHz continuum images of the 16 continuum-detected CARMA GOALS objects. The field of view is equivalent to what was used in Figures 2 and 3. In most cases, the continuum is unresolved by CARMA.

where $t_{\rm exp}$ is the exposure time in seconds, while $m_{g,r,i}$, $ct_{g,r,i}$, and $f_{g,r,i}$ are the magnitude, count, and flux in Jansky for the g, r, and i filters, respectively. A foreground extinction was subsequently applied in the same manner as was done for the GALEX photometry but directly using the extinction magnitudes from E. F. Schlafly & D. P. Finkbeiner (2011) provided by NED. Photometric errors in these images dominated the uncertainty and were conservatively estimated at the 10% level.

Since the optical images from PanSTARRS have sufficient spatial resolution to resolve the large-scale tidal features of each merger system, we employed mask photometry to properly measure the total flux within these optical bands. Specifically, masks have been generated based on isophotes of 24.5 mag in the PanSTARRS i-band images for consistent comparisons to the global optical fluxes from previous GOALS studies (J. H. Howell et al. 2010; T. Vavilkin 2011; U V. et al. 2012). Within the wavelength regime covered by the PanSTARRS filters, the masks are much larger than the molecular gas footprint, and hence aperture corrections are not needed in these bands. The mask apertures generally cover similar regions to those used for the other bands, yielding photometry consistent within the errors with that derived using the elliptical aperture from the other bands.

3.2.3. 2MASS Photometry

All of our galaxies were observed as part of 2MASS. We retrieved mosaics for the 11 galaxies not included in V. U et al. (2012) from the NASA/IPAC Infrared Science Archive (IRSA). Using the magnitude zero-points given in the header of each image, we converted the background-subtracted counts, measured in the same aperture as the GALEX fluxes, to magnitudes and then to fluxes using the conversions of M. Cohen et al. (2003). Background estimates were measured using source-free regions near each galaxy, and photometric uncertainties are the sum in quadrature of Poisson uncertainty, uncertainty due to uncertainty in the flux conversion factor, and a 3% calibration uncertainty (R. Cutri et al. 2006).

3.2.4. Spitzer Photometry

In the MIR, we used photometry from the Infrared Array Camera (IRAC; G. G. Fazio et al. 2004) and the 24 μm band of the Multiband Imaging Photometer (MIPS; G. H. Rieke et al. 2004) on Spitzer. Mosaics generated via the automatic pipeline were retrieved from the Spitzer Heritage Archive. Using the same aperture as the GALEX and 2MASS photometry, we calculated background-subtracted fluxes. We used the extended source aperture corrections given in the instrument handbooks,[34] using the effective radius of the elliptical aperture given by the geometrical mean of its axes. Photometric uncertainties consist of the sum in quadrature of the calibration uncertainty (3% for IRAC, M. Cohen et al. 2003; 4% for MIPS, C. W. Engelbracht et al. 2007) and the error measured on the uncertainty mosaics.

3.3. SED Fitting

Because at least 11/28 of the CARMA GOALS sources contain AGNs, we used two, related SED fitting codes to extract galactic properties from their broadband photometry: MAGPHYS(E. da Cunha et al. 2008), which is an SED fitting code that balances energy, and SED3FIT (S. Berta et al. 2013), a modified version of MAGPHYS that also includes AGN templates. The sections below summarize the two fitting programs.

The decision to include an AGN component in the SED fitting was based on the AGN diagnostics in A. O. Petric et al. (2011), which determined the AGN contribution using MIR emission. If this fraction was above 0, we identified the system as an AGN composite. We also double-checked these determinations in the χ^2 from fitting with MAGPHYS only versus SED3FIT. Additionally, an AGN component was included for NGC 4922, which is a Seyfert 2 galaxy (M. L. Saade et al. 2022), because the SED fit is significantly improved with an AGN component.

3.3.1. Magphys

MAGPHYS[35](DCE08) uses a physically motivated approach, balancing the UV-optical radiation from stars absorbed by dust and its reradiation in the FIR. These two wavelength regimes are covered by separate model libraries combined via this energy balance. The stellar UV–NIR library contains 50,000 spectral models generated via the population synthesis code of G. Bruzual & S. Charlot (2003) assuming an exponentially declining star formation history (SFH) onto which random bursts are superimposed (creating stochastic SFHs). These 50,000 spectra cover a wide range of parameters, including number and timing of SF bursts, dust mass (and attenuation), metallicity, and stellar mass. For each SFH, the average SFR over the last 10 Myr and 100 Myr are calculated. Attenuation by dust on these stellar models is implemented using the two-component model of S. Charlot & S. M. Fall (2000), which

---

[34] http://irsa.ipac.caltech.edu/data/SPITZER/docs/irac/iracinstrumenthandbook/29/ and https://irsa.ipac.caltech.edu/data/SPITZER/docs/mips/mipsinstrumenthandbook/50/

[35] The E. da Cunha et al. (2008) models are publicly available as a user-friendly model package MAGPHYS at www.iap.fr/magphys/.

uses a larger attenuation for stars in birth clouds relative to attenuation by the ambient ISM for older stars.

The dust emission is also modeled with a library of 50,000 IR spectra, composed out of four different components. Denser ISM associated with stellar birth clouds consists of polycyclic aromatic hydrocarbons (PAHs), stochastically-heated hot dust (temperatures of 130−250 K), and warm dust (30−60 K) in thermal equilibrium. PAH emission is modeled with a fixed template derived from observations of nearby star-forming galaxies, while the two dust components are modeled as graybody emission. For the diffuse ambient ISM, the relative fractions of these three components are fixed and an additional cold dust (15−25 K) component is included. MAGPHYS assumes a dust mass absorption coefficient $\kappa_\lambda \propto \lambda^{-\beta}$ which has a normalization of $\kappa_{850} = 0.077\ \mathrm{m^2\ kg^{-1}}$. A dust emissivity index of $\beta = 1.5$ is assumed for warm dust and $\beta = 2.0$ for cold dust.

MAGPHYS uses a Bayesian approach to determine the likelihood that models paired by the energy balance requirement could generate the observed photometry. Model photometry is generated using the response functions for the observed filters. Probability density functions (PDFs) are generated for parameters of interest by marginalizing over the other parameters. We plot these for the average SFR in the last 10 Myr as insets in Figure 6.

3.3.2. SED3FIT

SED3FIT (S. Berta et al. 2013) is a variant on MAGPHYS with an additional set of AGN torus templates based on the updated J. Fritz et al. (2006) models described in A. Feltre et al. (2012). These models cover a range of lines of sight (0°−90°) through a variety of equatorial optical depths (0.1−6). Torus parameters, including outer and inner radii and aperture angle, are held fixed at values of $R_{\rm out}/R_{\rm in} = 30°$ and 40°, respectively. The density distribution along the horizontal and vertical axes and the slope of the power law in the NIR–MIR domain are all held fixed at zero. Due to the additional parameter space added by these models, using the full set of models can quickly become computationally expensive. We therefore reach a compromise between run time and sampling of the prior space and run the code with 10,000 optical, 1000 IR, and 10 torus model libraries randomly drawn from the full sample. Statistical constraints are obtained in the same way as MAGPHYS, but with the additional torus parameters. In this work, we limit our analysis to the fraction of IR luminosity, $L(8-1000\ \mu\mathrm{m})$, from the torus component. For galaxies in which the AGN component significantly improves the fit, Figure 6 shows the fit both with and without the AGN component, and we include the PDF of the fraction of the IR luminosity contributed by the torus.

4. Molecular Gas Properties of CARMA GOALS Galaxies

To derive molecular gas properties, we convert the CO luminosity to a molecular gas mass (including helium) assuming a Milky Way-like $L_{\rm CO}/M({\rm H_2})$ conversion (A. D. Bolatto et al. 2013). It was argued in D. Downes & P. M. Solomon (1998) that the standard conversion often overestimates of the total molecular gas mass in interacting galaxies, due in part to the disrupted nature of the gas. This leads to a different distribution of molecular gas than in the Milky Way and similar galaxies. Namely, there is a substantial fraction of molecular gas in a diffuse component within interacting galaxies, rather than the conglomeration of finite clumps and molecular complexes like in the Milky Way (and by extension, normal star-forming galaxies). Given this fact, converting from $L_{\rm CO}$ to $M({\rm H_2})$ is not clear cut and the conversion factor for each individual galaxy may be different (rather than being able to make assumptions over the whole of the population.)

5. Discussion

5.1. The Nature of the 100 GHz Continuum

Mergers and interactions have a high incidence of AGN activity (J. E. Barnes & L. Hernquist 1992; J. Kormendy & L. C. Ho 2013). Despite this, these AGN can be difficult to detect due to the extreme (and often Compton thick) column densities that often obscure the AGN. For this reason, traditional searches including optical emission line ratios and even X-rays can sometimes fall short. In the era of Spitzer, identifying AGN in these circumstances became simpler, due to the fact that the hot dust radiating from the accretion disk and torus region influence the MIR colors (D. Stern et al. 2005, 2012; M. Lacy et al. 2007, 2013). MIR spectroscopy is an even more powerful diagnostic, with MIR lines that can unambiguously identify AGN and being far less affected by extinction (A. O. Petric et al. 2011). While the MIR selection is powerful, if an AGN is present but not radiatively dominant, especially when buried under dense gas, these methods can also fail to detect an AGN's presence.

T. Kawamuro et al. (2022) investigated a large sample of AGN using ALMA, focusing on the $\lambda \approx 1$ mm regime. They found that there is significant emission, and that the emission cannot be explained as originating from star formation, and must originate from the ultracompact coronae of the AGN, and that there was a clear correlation with the AGN luminosity. This leads to the possibility that compact millimeter continuum might be an independent tracer of AGN activity, including in sources with star formation dominating the IR emission, and Compton thick molecular gas columns obscuring the hard X-rays. Our result is consistent with the findings of C. Ricci et al. (2023) of a definitive connection between bright compact millimeter emission and AGN activity. All of our sources except for one (NGC 958) are detected in the VLA Sky Survey (VLASS; M. Lacy et al. 2020). However, it is nontrivial to unambiguously distinguish between AGN jet and star formation origins for the radio continuum emission using only the VLASS data.

In many of our CARMA GOALS sources, the correlator setup available for our observations allowed us to measure radio continuum in conjunction with the molecular line emission, which we were able to detect and image in 16 of our sources. Figure 5 presents the imaging of the 100 GHz continuum for these sources. We note that the majority of the 3 mm continuum sources are unresolved, consistent with an AGN origin. But it is also possible that in many cases we are tracing ultracompact starbursting regions. In order to test this hypothesis, we convert the 100 GHz emission to a SFR using Equation (10) from E. J. Murphy et al. (2012); assuming that 100 GHz emission originates from star formation. Figure 7 presents a comparison between the 100 GHz SFRs and the SED fit SFRs. We see that in the case for all but three sources (IRAS 03582+6012, Arp 55 and VV 250), the 100 GHz

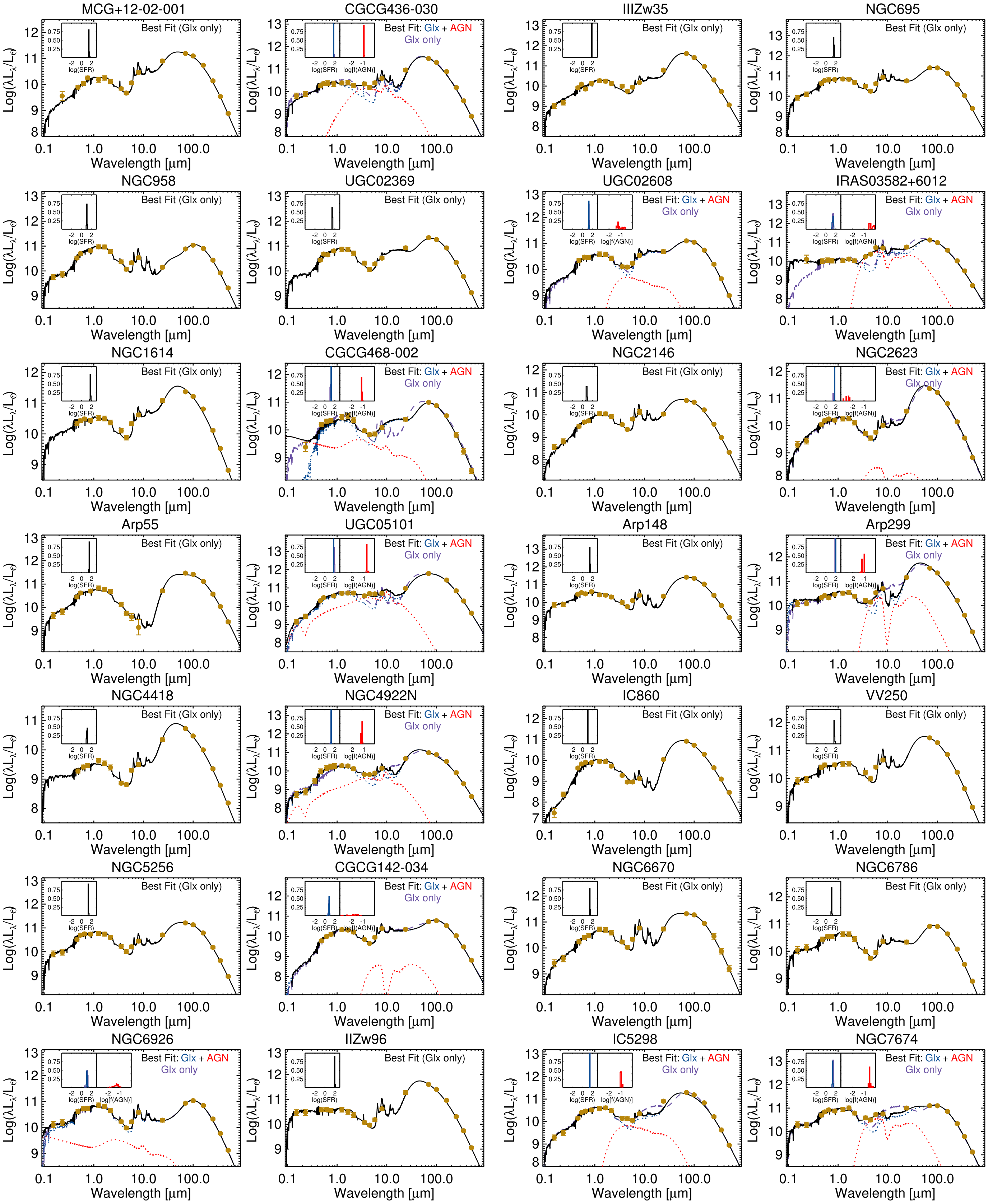

Figure 6. Best-fitting models to the SEDs. The black line shows the best overall model. In some cases, the fit was improved by including a torus component from the AGN (shown in red) in addition to the galactic emission (shown in blue). The fit achieved with just galactic emission in those cases is shown in purple. See Section 3.3 for discussion on the fitting process. PDFs for SFR in the last 10 Myr and, as relevant, fraction of IR luminosity arising from the AGN component are shown as insets. When a galaxy is modeled both with and without an AGN component, both of the resulting SFR PDFs are shown. These generally do not show much difference, indicating that the inclusion of an AGN component does not affect our derived SFR significantly.

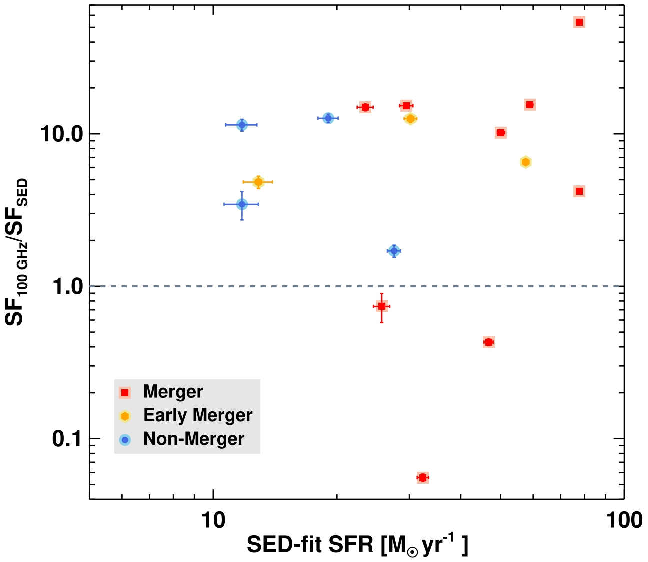

Figure 7. The ratio between the SF predicted by the 100 GHz continuum and SED fitting, showing that for the majority of the these sources, the 100 GHz emission cannot come from a star formation origin.

derived SFRs exceed the MAGPHYS-derived SFRs by factors of at least 2, and up to 50. This suggests that in many cases the 100 GHz emission cannot come from a star formation origin, and must instead be from an alternative.

A. O. Petric et al. (2011) measured AGN contributions to the MIR for the GOALS sample, including all 16 of our 100 GHz detected sources. They found AGN contributions in all except for MCG+12-02-001, NGC 1614, NGC 4418, and VV 250. This points to an AGN origin for much of the 100 GHz emission that we measure, though given that these sources are all LIRGs and ULIRGs, we also cannot rule out that the Rayleigh–Jeans tail of dust emission is also contributing to these detections. While we find a ratio of SFR$_{100}$/SFR$_{\mathrm{SED}}$ of 15 for NGC 1614, S. König et al. (2016) used ALMA to observe NGC 1614, and found the 3 mm continuum region to be centrally peaked, but with components that traced the dust lanes and CO emission as well. This points to there being multiple origins of the 100 GHz emission in CARMA GOALS sources, and suggests that in this sample a clean separation of emission from the AGN and star formation is difficult due to their substantial molecular reservoirs, significant star formation activity, and opaque column densities, even into the X-rays.

Higher resolution 100 GHz continuum measurement will be able to spatially distinguish between emission originating from star formation and the AGN, as was done in S. König et al. (2016), but that is beyond the scope of this paper.

5.2. Morphologies of the Molecular Gas

If we focus on the spectra (Figure 4), we observe a large variety of shapes. In many objects, we see the familiar double-horned profile consistent with the molecular gas tracing the rotation out to the flat part of the rotation curve. Other spectra show Gaussian-dominated profiles, although in many cases these are the objects with 80 km s^{-1} channel widths, which likely resolve out some of the subcomponents of the velocity. Originally, we may have assumed that these Gaussian profiles were observed in objects with significant amounts of disordered, turbulence-dominated molecular gas, but the average velocity maps (Figure 3) reveal different properties. The vast majority of CARMA GOALS sources show clear velocity gradients, likely representing that the molecular gas is overall rotation dominated. Even in galaxies that are at end-stages of mergers, there is ordered motion in the molecular gas. This result is consistent with J. Ueda et al. (2014), which also found that the majority of merger remnants exhibited ordered motion in their molecular gas velocity profiles. It is possible that this signifies that the molecular gas rapidly resettles into a disk configuration, even while other signs of morphological disruption remain at other wavelengths. This means that the presence of velocity gradients in high-redshift galaxies and submillimeter galaxies (R. Genzel et al. 2020; F. Stanley et al. 2023) does not imply that they are dynamically settled systems, as one might have assumed from the rotation domination observed in the gas.

The moment maps and distributions of the CARMA data shown in Figures 1–3 display the various gas morphologies present in our sample. Although the majority of sources show signs of order and rotation, 11/28 sources are disordered (III Zw 35, Arp 299W, NGC 4418) or have abnormal gas components (NGC 695, UGC 02369, NGC 2623, NGC 4922, NGC 5256), and some show molecular bridges between two components (IRAS 03582+6012, Arp 55, II Zw 96). While many of these disrupted gas morphologies appear in galaxies classified as mergers (S. Stierwalt et al. 2014; K. L. Larson et al. 2016; A. O. Petric et al. 2018), there are at least a few that are found in either early-merger or nonmerging galaxies (II Zw 35, IC 860, NGC 4418), suggesting that the disruption in the molecular gas does not necessarily perfectly match the optical or IR morphological characteristics of the system.

In those cases where there is no obvious merger, the disrupted molecular gas may be pointing to a previous merger event or a minor merger (K. Alatalo et al. 2014), where the dense molecular gas has been driven into the center and is igniting star formation and/or an AGN, which in turn is creating the substantial IR flux that is observed. Indeed, both IC 860 and NGC 4418 are known to be compact obscured nuclei (CONs; N. Falstad et al. 2021), it is probable that the AGN in these obscured sources is not only providing additional radiative power that we observe in the IR but is also stirring up the molecular gas.

5.3. The Gas to Dust Ratio of CARMA GOALS Sources

The ratio of dust mass to gas mass in galaxies is thought to fit into a small range of values, as has been seen in star-forming galaxies (K. M. Sandstrom et al. 2013), ranging from 43 to 120, for galaxies with solar metallicities. Previous studies of ULIRGs have used this range of values to calibrate the conversion between L_{CO} and $M(\mathrm{H}_2)$ (R. Herrero-Illana et al. 2019). This method takes into account the fact that ULIRGs and LIRGs have a different distribution of molecular gas than is seen in either the Milky Way, the most commonly used α_{CO} calibrator, or normal star-forming galaxies (D. Downes & P. M. Solomon 1998).

Figure 8 shows the gas-to-dust ratios for the CARMA GOALS sources. Dust masses were calculated using MAGPHYS (or in the cases of galaxies with significant AGN contributions, SED3fit), as discussed in Section 3.3. Gas masses were calculated using different assumptions for α_{CO}, including a Milky Way conversion, as well as the α_{CO} found by R. Herrero-Illana et al. (2019) to be appropriate for GOALS sources. Assuming a Milky

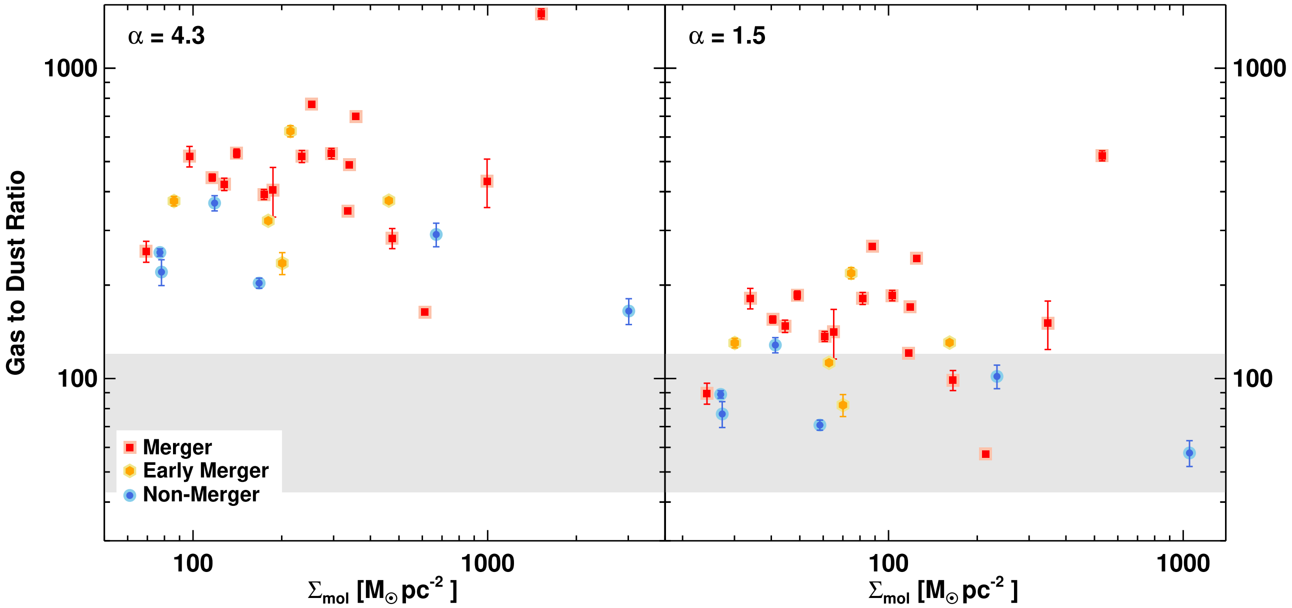

Figure 8. The gas-to-dust ratio for all CARMA GOALS sources labeled based on their merger classification from A. O. Petric et al. (2018): red squares for "m"/mergers, orange hexagons for "em"/early-mergers, and blue circles for "nm"/nonmergers. With the left-hand plot using the standard Milky Way conversion factor ($\alpha = 4$). The range of gas-to-dust ratios for normal star-forming galaxies from K. M. Sandstrom et al. (2013) is shaded in gray. If we assume that $L_{\rm CO}$-to-$M(\rm H_2)$ conversion is not consistent with a Milky Way conversion and use the conversion from R. Herrero-Illana et al. (2019), we find that the measured gas-to-dust ratios in our sources are much more consistent with the range found in normal galaxies. The plot on the right-hand side uses the $\alpha_{\rm CO}$ determined for GOALS sources in R. Herrero-Illana et al. (2019).

Way conversion of 4.3 $M_\odot$ (K km s^{-1} pc^2)$^{-1}$, we find that the gas-to-dust ratio of the CARMA GOALS sources ranges between 164 and 1500, which is significantly higher than the range of ratios seen in star-forming galaxies. Using the R. Herrero-Illana et al. (2019) value of 1.5 $M_\odot$ (K km s^{-1} pc^2)$^{-1}$, the gas-to-dust ratio ranges between 57 and 522, which while still higher than what is seen in the star-forming sample span a much more reasonable set of values.

Although this adopted value does not completely reconcile the CARMA GOALS sources and star-forming galaxies, it is possible that these sources have an intrinsically higher gas-to-dust ratio than star-forming galaxies. Most of the CARMA GOALS sources have undergone an interaction, allowing shocks to pass through the dense gas and dust, destroying a non-negligible amount of the dust in their wake. Figure 8 also codifies the merger classification from A. O. Petric et al. (2018), including mergers, early mergers, and nonmergers. What we see is no matter the $\alpha_{\rm CO}$ chosen, mergers tend to have the highest gas-to-dust ratios, with a median gas-to-dust of 444, followed by early mergers (368) and nonmergers (254). This supports the idea that the molecular gas is more stirred up during a collision, possibly producing both effects that are seen: less dust and more diffuse gas, which would require a lower $\alpha_{\rm CO}$. Indeed, F. Renaud et al. (2019) argue that $\alpha_{\rm CO}$ varies depending on the merger phase and state of the molecular gas throughout the merger sequence, which our results support. Because both of these effects are likely present, it is difficult to disentangle one from the other. It would require extremely high resolution observations (i.e., those capable of resolving the scale height of the galaxy) that are able to trace the dust distribution, as well as map the velocity dispersion of the molecular gas to determine which is the source of this elevated ratio. Despite this, we are able to look at other properties of the molecular gas in these galaxies to provide us with additional information. We will revisit the gas-to-dust ratio in Section 5.5.

5.4. The Molecular Gas Fraction of CARMA GOALS Sources

We define the molecular gas fraction as the ratio between molecular gas mass and stellar mass:

$$f_{\rm mol} = \frac{M_{\rm mol}}{M_{\rm mol} + M_\star}.$$

There are many properties in these sources that naturally fall out of the assumptions we make when determining the proper conversion from $L_{\rm CO}$ and $\rm H_2$ mass, including the molecular gas fractions that we measure in these systems. Indeed, if we were to use the Milky Way conversion, there are many cases where the molecular gas mass would exceed the stellar mass ($f_{\rm mol} \gtrsim 0.5$), which while not impossible is not common, even in the most gas-rich mergers at low redshift (D. Downes & P. M. Solomon 1998). Therefore, we have adopted $\alpha_{\rm CO} = 1.5$, which is consistent with the value found from R. Herrero-Illana et al. (2019) for these sources.

We present the molecular gas fractions, derived from the stellar mass found in Table 3 and the molecular gas mass found in Table 4, in Figure 9. There are two trends visible in this plot: the first is that the molecular gas fraction correlates with SFR. Given that the stellar mass of these objects occupies a similar range, this result can be explained since more molecular gas naturally elicits more star formation. The second trend that we observe in this plot is that molecular gas fraction also correlates with merger stage, where those objects classified morphologically as being mergers are far more likely to have high molecular gas fractions and those that are classified as nonmergers also have lower molecular gas fractions. Indeed, even when accounting for SFRs, nonmergers tended to have lower molecular gas fractions than mergers (D. Iono et al. 2004). It is well known from simulations that the molecular gas

Table 3
CARMA GOALS MAGPHYS Properties

Name (1)	χ^2 (2)	$\log_{10}(M_*)$ (3)	$\log_{10}(M_{\rm dust})$ (4)	$\log_{10}(L_{\rm dust})$ (5)	$\log_{10}$(SFR) (6)	flag_agn (7)
MCG+12-02-001	32.79	$10.48^{+0.25}_{-0.23}$	$7.8^{+0.0}_{-0.03}$	$11.49^{+0.0}_{-0.02}$	$1.47^{+0.04}_{-0.04}$	0
CGCG 436-030	61.08	$10.4^{+0.0}_{-0.0}$	$7.67^{+0.0}_{-0.0}$	$11.66^{+0.0}_{-0.0}$	$1.76^{+0.0}_{-0.04}$	1
III Zw 35	70.54	$10.61^{+0.02}_{-0.0}$	$7.79^{+0.0}_{-0.0}$	$11.72^{+0.01}_{-0.0}$	$1.82^{+0.01}_{-0.0}$	0
NGC 695	20.39	$10.92^{+0.12}_{-0.07}$	$8.26^{+0.03}_{-0.04}$	$11.68^{+0.01}_{-0.02}$	$1.59^{+0.03}_{-0.05}$	0
NGC 958	8.95	$11.28^{+0.08}_{-0.1}$	$8.3^{+0.03}_{-0.05}$	$11.25^{+0.01}_{-0.01}$	$1.06^{+0.04}_{-0.05}$	0
UGC 02369	28.55	$11.11^{+0.1}_{-0.11}$	$7.99^{+0.01}_{-0.04}$	$11.57^{+0.02}_{-0.02}$	$1.48^{+0.09}_{-0.06}$	0
UGC 02608	11.58	$10.59^{+0.12}_{-0.06}$	$7.87^{+0.02}_{-0.01}$	$11.38^{+0.01}_{-0.04}$	$1.28^{+0.03}_{-0.02}$	1
IRAS 03582+6012	36.5	$9.85^{+0.09}_{-0.17}$	$7.61^{+0.02}_{-0.04}$	$11.32^{+0.08}_{-0.09}$	$1.41^{+0.07}_{-0.04}$	1
NGC 1614	66.38	$10.24^{+0.52}_{-0.0}$	$7.62^{+0.03}_{-0.0}$	$11.7^{+0.0}_{-0.05}$	$1.77^{+0.02}_{-0.0}$	0
CGCG 468-002	35.84	$10.57^{+0.0}_{-0.0}$	$7.46^{+0.0}_{-0.0}$	$11.15^{+0.0}_{-0.0}$	$1.11^{+0.02}_{-0.02}$	1
NGC 2146	28.86	$10.28^{+0.12}_{-0.14}$	$7.27^{+0.02}_{-0.02}$	$10.91^{+0.01}_{-0.01}$	$0.81^{+0.06}_{-0.06}$	0
NGC 2623	90.42	$10.52^{+0.0}_{-0.0}$	$7.75^{+0.0}_{-0.0}$	$11.57^{+0.0}_{-0.0}$	$1.7^{+0.0}_{-0.21}$	1
Arp 55	47.62	$10.83^{+0.07}_{-0.04}$	$8.3^{+0.0}_{-0.0}$	$11.64^{+0.0}_{-0.01}$	$1.51^{+0.01}_{-0.01}$	0
UGC 05101	25.87	$10.92^{+0.0}_{-0.02}$	$8.51^{+0.0}_{-0.02}$	$11.95^{+0.0}_{-0.02}$	$1.89^{+0.04}_{-0.01}$	1
Arp 148	52.75	$10.42^{+0.04}_{-0.06}$	$8.03^{+0.0}_{-0.01}$	$11.56^{+0.0}_{-0.0}$	$1.47^{+0.05}_{-0.01}$	0
Arp 299	51.94	$10.77^{+0.0}_{-0.0}$	$7.75^{+0.0}_{-0.0}$	$11.83^{+0.01}_{-0.0}$	$1.89^{+0.0}_{-0.0}$	1
NGC 4418	26.7	$9.68^{+0.26}_{-0.24}$	$6.91^{+0.1}_{-0.02}$	$11.0^{+0.01}_{-0.07}$	$1.07^{+0.05}_{-0.06}$	0
NGC 4922N	48.74	$10.41^{+0.0}_{-0.0}$	$7.62^{+0.0}_{-0.0}$	$11.28^{+0.0}_{-0.0}$	$1.21^{+0.08}_{-0.01}$	1
IC 860	104.98	$10.47^{+0.0}_{-0.0}$	$7.21^{+0.0}_{-0.0}$	$11.03^{+0.0}_{-0.01}$	$1.07^{+0.0}_{-0.01}$	0
VV 250	40.91	$10.33^{+0.26}_{-0.06}$	$7.82^{+0.0}_{-0.04}$	$11.66^{+0.03}_{-0.01}$	$1.67^{+0.08}_{-0.03}$	0
NGC 5256	22.52	$10.87^{+0.09}_{-0.07}$	$7.84^{+0.01}_{-0.0}$	$11.46^{+0.0}_{-0.01}$	$1.37^{+0.02}_{-0.02}$	0
CGCG 142-034	9.96	$10.79^{+0.08}_{-0.12}$	$7.71^{+0.05}_{-0.01}$	$11.06^{+0.02}_{-0.01}$	$0.81^{+0.07}_{-0.07}$	1
NGC 6670	11.87	$10.88^{+0.12}_{-0.13}$	$8.12^{+0.09}_{-0.05}$	$11.59^{+0.01}_{-0.03}$	$1.47^{+0.04}_{-0.04}$	0
NGC 6786	6.36	$10.6^{+0.13}_{-0.12}$	$7.76^{+0.02}_{-0.0}$	$11.17^{+0.01}_{-0.01}$	$1.15^{+0.03}_{-0.04}$	0
NGC 6926	11.29	$11.02^{+0.05}_{-0.12}$	$8.05^{+0.04}_{-0.03}$	$11.25^{+0.01}_{-0.01}$	$1.17^{+0.06}_{-0.05}$	1
II Zw 96	37.4	$10.22^{+0.21}_{-0.3}$	$7.88^{+0.01}_{-0.09}$	$11.87^{+0.0}_{-0.03}$	$1.94^{+0.03}_{-0.02}$	0
IC 5298	83.5	$11.15^{+0.0}_{-0.0}$	$7.84^{+0.0}_{-0.0}$	$11.44^{+0.0}_{-0.0}$	$1.44^{+0.01}_{-0.0}$	1
NGC 7674	17.82	$11.01^{+0.04}_{-0.0}$	$8.04^{+0.0}_{-0.04}$	$11.44^{+0.0}_{-0.02}$	$1.48^{+0.03}_{-0.02}$	1

Note. Column (1): Object name. Column (2): Best fit χ^2. Column (3): Stellar mass. Column (4): Dust mass. Column (5): Dust luminosity. Column (6): SFR averaged over the last 10^7 yr. Uncertainties are indicated by the median 84th–16th percentile range from each individual parameter PDF. Column (7): AGN flag.

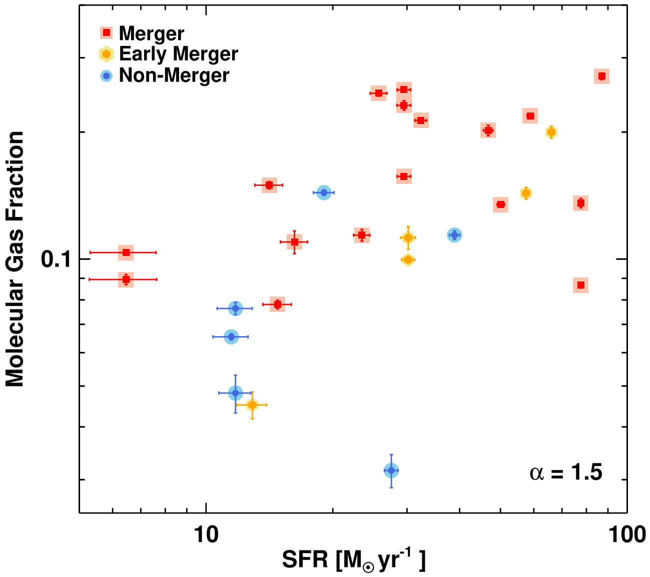

Figure 9. The molecular gas fraction for all the CARMA GOALs sources, labeled based on their merger classification from A. O. Petric et al. (2018): red squares for "m"/mergers, orange hexagons for "em"/early-mergers, and blue circles for "nm"/nonmergers. There is a noticeable trend that higher SFRs also contain higher molecular gas fractions.

fraction increases as a merger progresses (P. F. Hopkins et al. 2008; H. He et al. 2023), so our results are unsurprising.

5.5. The Star Formation Efficiency of CARMA GOALS Sources

In order to compare the star formation–molecular gas surface densities, we use the values derived for star formation via fitting of SEDs composed of ultraviolet (UV) to far-infrared (FIR) photometry, described in detail in Section 3.3. We calculate the molecular gas mass using the CO luminosities presented in Table 2 and then assume a conversion factor informed by the gas-to-dust ratio results from Section 5.3 of $\alpha_{\rm CO} = 1.5$, which corresponds to $M({\rm H_2})/M_\odot = 3.1 \times 10^4\, L_{\rm CO}/L_\odot$. Finally, we use the footprint of the molecular gas present in the moment0 maps to determine the total area subtended by the molecular gas. Because the observations used for SED fitting includes wave bands in which the source is unresolved (e.g., FIR), we assume cospatiality of star formation and molecular gas. Figure 10 shows the CO intensity maps overlaid on a three-color Spitzer image of each galaxy (the 8 μm feature represented as red). The 7.7 μm PAH feature, which is present in the 8 μm broadband filter, traces the gas remarkably well. If we assume that this feature is primarily tracing star formation in these systems (D. Calzetti et al. 2007; T. Díaz-Santos et al. 2011), then cospatiality is an appropriate assumption to make.

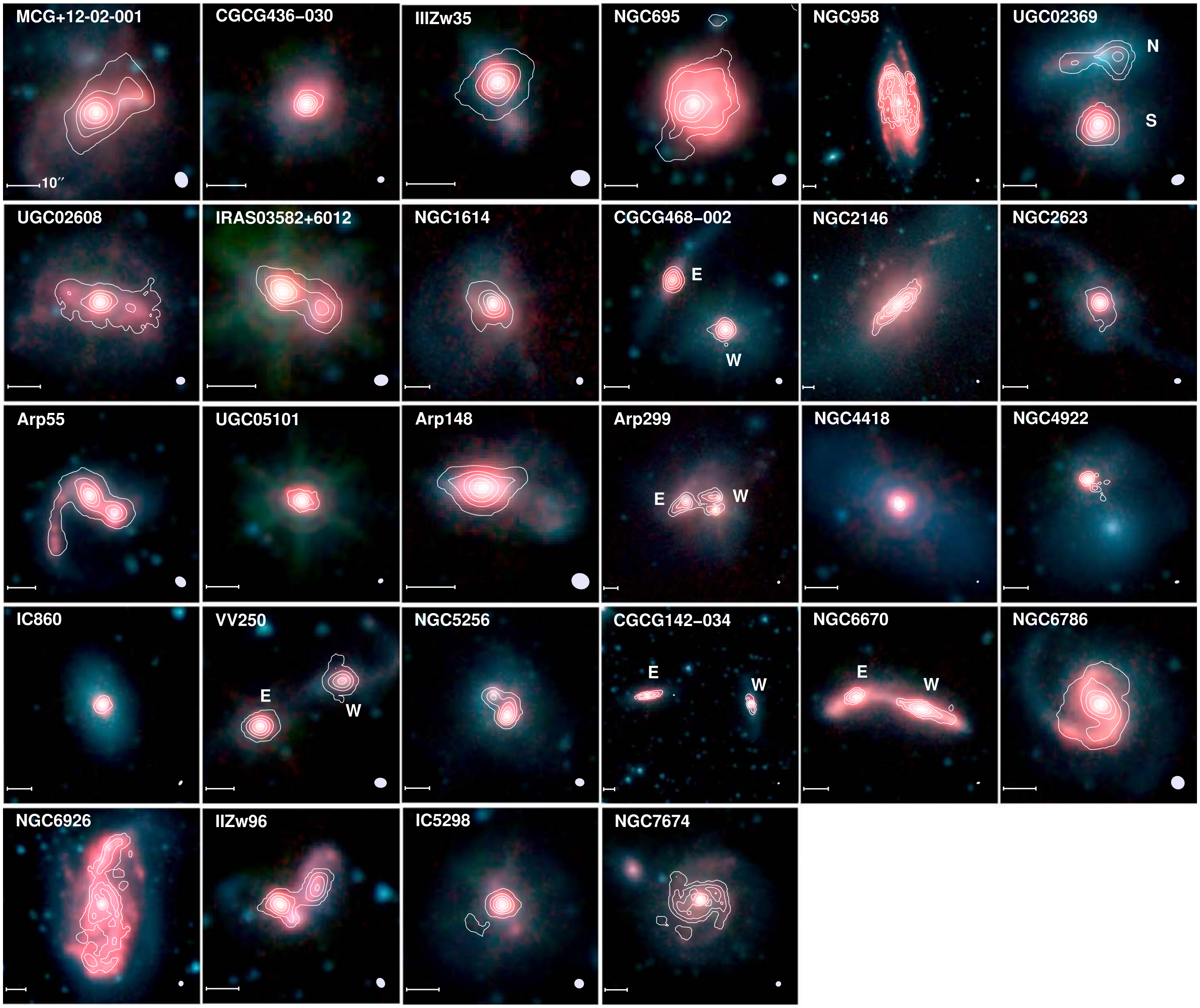

Figure 10. The moment0 maps of CO(1–0) of the 28 CARMA GOALS galaxies overlaid atop the three-color Spitzer 3.6–4.5–8.0 μm image. The white bar in the lower left-hand corner demarcates 10″ in each field. The beam is shown in the lower right-hand corner in white. The red-hued portions of the Spitzer map show the locations of the PAH emission, which matches the positions of the molecular gas quite well.

Figure 11 shows the CARMA GOALS sample placed on Schmidt–Kennicutt relation (S-K; M. Schmidt 1959; R.C. Kennicutt 1998), along with comparison samples, including normal star-forming galaxies (R. C. Kennicutt 1998; D. B. Fisher et al. 2013), bulges (D. B. Fisher et al. 2013), early-type galaxies (T. A. Davis et al. 2014), Hickson Compact Group galaxies (K. Alatalo et al. 2015a), high-redshift galaxies (R. Genzel et al. 2010), and radio galaxies (P. Ogle et al. 2010), all renormalized to a common G. Chabrier (2003) initial mass function. We have also color-coded each CARMA GOALS source with its gas-to-dust ratio. On average, CARMA GOALS sources are found to be above the "standard" relation and in comparison to the selected samples but still well within the scatter. This suggests that the star formation in these sources is superefficient (e.g., that more stars are forming in a given period of time than is seen in normal star-forming galaxies and the other comparisons we have made). There are many possible explanations for this. First, this could be a result of the conversion factor that we have chosen. If we assumed a conversion factor more in line with what is observed in the Milky Way or normal star-forming galaxies (K. M. Sandstrom et al. 2013), then these points would fall much closer to the average relation. While it is not improbable that some dust has been destroyed during the interaction, which could lead to an enhanced gas-to-dust ratio in these sources, it is much more likely that the diffuse component of the molecular gas compensates for this dust destruction, so it is less likely that our enhanced star formation efficiency in these sources can be explained simply as a misconversion.

It is worth considering that in these sources the star formation efficiency is higher. M. R. Krumholz et al. (2012) laid the theoretical groundwork to explain the S-K relation, in that approximately 1% of dense gas is converted into stars per freefall time. D. M. Salim et al. (2015) took this concept further, showing that the Mach number also has influence on the star formation efficiency by modifying the freefall time. In

Table 4
CARMA GOALS Derived Properties

Name (1)	$M(H_2)$ ($10^9\ M_\odot$) (2)	Σ_{H_2} ($M_\odot$ pc^{-2}) (3)
MCG+12-02-001	8.63 ± 0.01	174.1 ± 0.3
CGCG 436-030	6.11 ± 0.03	461.9 ± 2.1
III Zw 35	7.96 ± 0.05	180.0 ± 1.2
NGC 695	16.18 ± 0.04	77.21 ± 0.2
NGC 958	15.34 ± 0.02	78.14 ± 0.09
UGC 2369N	7.36 ± 0.11	140.4 ± 2.0
UGC 2369S	14.00 ± 0.11	295.6 ± 2.2
UGC 02608	9.51 ± 0.02	118.4 ± 0.3
IRAS 03582 + 6012	6.01 ± 0.02	127.7 ± 0.5
NGC 1614	10.17 ± 0.01	357.1 ± 0.4
CGCG 468-002W	1.15 ± 0.01	150.3 ± 1.
CGCG 468-002E	2.04 ± 0.01	247.6 ± 0.9
NGC 2146	2.81 ± 0.01	995.3 ± 0.6
NGC 2623	6.78 ± 0.01	339.1 ± 0.5
Arp 55	37.03 ± 0.08	140.6 ± 0.3
UGC 05101	18.49 ± 0.06	612.2 ± 2.1
Arp 148	17.28 ± 0.10	295.1 ± 1.8
Arp 299W	4.18 ± 0.01	463.5 ± 0.7
Arp 299E	2.61 ± 0.01	232.9 ± 0.6
NGC 4418	0.468 ± 0.01	3011.6 ± 7.7
NGC 4922	4.12 ± 0.03	474.3 ± 3.2
IC 860	1.65 ± 0.01	668.9 ± 3.3
UGC 08335W	3.96 ± 0.04	84.84 ± 0.9
UGC 08335E	6.28 ± 0.04	151.3 ± 1.
NGC 5256	12.54 ± 0.05	234.1 ± 0.8
CGCG 142-034W	5.31 ± 0.01	331.7 ± 0.8
CGCG 142-034E	2.11 ± 0.01	88.94 ± 0.5
NGC 6670W	54.50 ± 0.07	1587.7 ± 2.0
NGC 6670E	14.35 ± 0.07	1314.2 ± 6.7
NGC 6786	10.44 ± 0.03	97.30 ± 0.3
NGC 6926	10.05 ± 0.02	69.36 ± 0.1
II Zw 96	20.24 ± 0.10	252.6 ± 1.3
IC 5298	4.90 ± 0.01	167.7 ± 0.5
NGC 7674	14.27 ± 0.02	86.19 ± 0.1

Note. Column (1): Object name. Column (2): H_2 mass derived from L_{CO} in units of $10^9\ M_\odot$ assuming $\alpha_{CO} = 1.5$ (R. Herrero-Illana et al. 2019). Column (3): H_2 surface density, or $M(H_2)$/area subtended by CO, in units of $M_\odot$ pc^{-2}.

this way, more turbulent systems will appear to have enhanced star formation efficiencies compared to normal star-forming galaxies when in reality the efficiency per freefall time is consistent. Interactions are well known to be turbulent systems (J. A. Rich et al. 2011; N. Lu et al. 2014; S. Stierwalt et al. 2014; D. Beaulieu et al. 2023), and CARMA GOALS sources are no exception. Thus, it is possible that the turbulence that has made a determination of the conversion factor more difficult has also impacted the freefall time of the star-forming gas, thus driving CARMA GOALS sources as a population "above" the S-K relation. In order to delve deeper into this question, an accurate determination of the intrinsic velocity dispersion of the molecular gas is necessary, which requires high resolution observations able to resolve the scale height of each galaxy, and is thus beyond the scope of this paper.

5.6. Molecular Inflows and Outflows in CARMA GOALS Galaxies

Multiple systems also show evidence of extended line wings (III Zw 35, UGC 02608, IRAS 03582+6012, NGC 1614, Arp 148, Arp 299, NGC 4418, IC 860, NGC 5256, II Zw 96). Some of these sources have confirmed AGN-driven molecular outflows already in the literature (NGC 1614; S. García-Burillo et al. 2015, III Zw 35; D. Lutz et al. 2020, IC 860; Y. Luo et al. 2022). In the case of NGC 4418, the wing may be associated with inflow of gas rather than outflow (F. Costagliola et al. 2013; E. González-Alfonso et al. 2015). In most cases, our CARMA-detected line wings are observed around ≈300 km s^{-1}, and often these wings are only seen on the redshifted or blueshifted side of the galaxy.

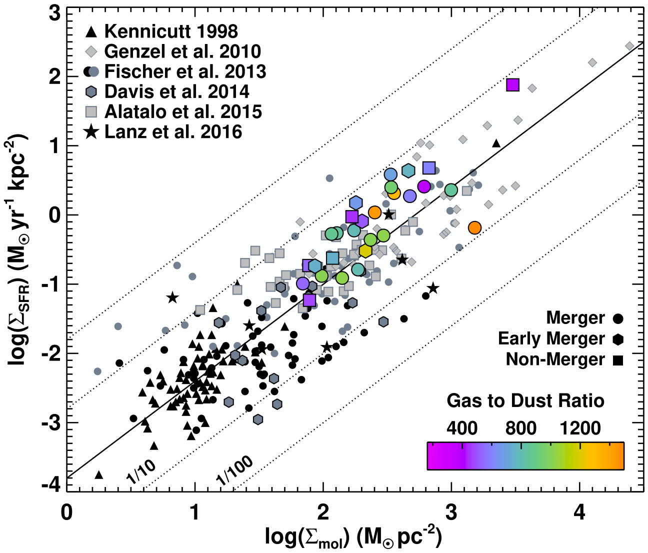

Figure 11. The Schmidt–Kennicutt relation (R.C. Kennicutt 1998) for the CARMA GOALS sample (color-coded by gas-to-dust ratio), with comparisons to normal star-forming galaxies (black triangles; R.C. Kennicutt 1998 and black circles; D. B. Fisher et al. 2013), bulges (gray circles; D. B. Fisher et al. 2013), early-type galaxies (teal squares; T. A. Davis et al. 2014), Hickson Compact Group galaxies (blue hexagons; K. Alatalo et al. 2015a), high-redshift galaxies (gray diamonds; R. Genzel et al. 2010), and radio galaxies (black squares; P. Ogle et al. 2010). The diagonal lines represent the 10× and 100× deviations from the average relation. All SFRs have been normalized to the Chabrier initial mass function (G. Chabrier 2003).

F. Peñaloza et al. (2023, in preparation) used ALMA Compact Array ($\theta_{fwhm} \approx 4\farcs7$) to study 18 LIRGs and ULIRGs from the GOALS sample and found that 12 of those 18 host molecular outflows involve more than 1% of their molecular mass, though at velocities below the escape velocity. Our results also support their claim that molecular outflows are common in interacting galaxies (something seen in ionized gas as well; C. M. Harrison et al. 2014), but that they are not a dominant mechanism in expelling the molecular gas. Indeed, it is possible that in these systems an AGN jet punching through the interstellar medium has a more significant impact on the depletion of the gas reservoir via star formation through the additional turbulence (and therefore shortened freefall time) than through the direct expulsion of the molecular gas, an effect that is seen in both Markarian 231 (K. Alatalo 2015) and NGC 1266 (K. Alatalo et al. 2015c).

6. Conclusions

We have presented observations of 28 LIRGs and ULIRGs that are part of the GOALS sample with CARMA, resolving all sources in CO(1–0).

1. We have detected 16 of the 28 sources in 100 GHz continuum, with the vast majority of those objects being unresolved. The SFRs inferred from the 100 GHz

emission is factors of 2–10 too high (as compared with SED fitting) to be explained by star formation alone, suggesting that in most cases an AGN contributes non-negligibly to the emission.

2. Many of the CARMA GOALS systems show velocity gradients despite undergoing significant interactions. This implies that an ordered gradient observed in the molecular gas does not imply ordered rotation in the system.
3. The gas-to-dust ratios in the CARMA GOALS sources are much higher than expected if we use a $L_{\rm CO}$ to $M({\rm H}_2)$ conversion from the Milky Way. We instead use the conversion derived by R. Herrero-Illana et al. (2019) for the CARMA GOALS sources. The gas-to-dust ratio is higher than what is seen in normal star-forming galaxies, but is consistent with the hypothesis that the turbulent medium in interacting galaxies may have destroyed some of the dust reservoir. This choice also influences the molecular gas fraction observed in these sources, which are in line with what is expected in interacting galaxies.
4. The CARMA GOALs sources as a group have an enhanced star formation efficiency, as shown on the S-K relation. While this could be due to underestimating the $\alpha_{\rm CO}$ conversion factor, it is more likely that the turbulence present in these interacting systems has increased the Mach number above what is observed in star-forming galaxies, thus decreasing the freefall time, and therefore boosting the perceived efficiency of star formation.
5. Several of the CARMA GOALS sources show evidence of extended line wings, suggesting the presence of molecular outflows in many, supporting a growing number of studies that show that these outflows are ubiquitous in systems with molecular gas proximate to the AGN. Despite their ubiquity, it does not appear that they play a substantial role in the depletion of molecular gas from these systems.

It is clear that the study of molecular gas in merging galaxies is able to shed light on many other physical processes that are taking place, including the interaction between turbulence and star formation, between the AGN and the host galaxy, and even the fundamental question of how a galaxy ultimately quenches its star formation, depletes its star-forming fuel, and evolves passively as a quiescent galaxy. Higher resolution molecular gas measurements capable of accurately determining the total molecular mass paired with resolved maps able to trace star formation uncontaminated will be able to further our understanding of the intricacies of this important phase in quenching galaxies.

Acknowledgments

We thank the anonymous referee for their excellent suggestions that have improved this manuscript. K.A. thanks the participants of the Behind the Curtain of Dust II in Sexten for enlightening conversations that have helped develop and improve this manuscript. Support for K.A. is provided by NASA through Hubble Fellowship grant #HST-HF2-51352.001 awarded by the Space Telescope Science Institute, which is operated by the Association of Universities for Research in Astronomy, Inc., for NASA, under contract NAS5-26555. E.T. acknowledges support from: ANID through Millennium Science Initiative Program NCN19_058, CATA-BASAL ACE210002 and FB210003, and FONDECYT Regular 1190818 and 1200495. Y.L. and A.P. acknowledge support from SOFIA grant #08-0226 (PI: Petric). Y.L. acknowledges support from the Space Telescope Science Institute Director's Discretionary Research Fund grant D0101.90281. J.A.O. acknowledges support from the Space Telescope Science Institute Director's Discretionary Research Fund grants D0101.90296 and D0101.90311. M.S. acknowledges support from the William H. Miller III Graduate Fellowship. V.U. acknowledges funding support from NSF Astronomy and Astrophysics Research Grant # AST-2408820, NASA Astrophysics Data Analysis Program (ADAP) grant # 80NSSC23K0750, and STScI grant # HST-AR-17063.005-A, HST-GO-17285.001-A, and JWST-GO-01717.001-A. A.M.M. acknowledges support from NASA ADAP grant #80NSSC23K0750 and from NSF AAG grant #2009416 and NSF CAREER grant #2239807.

Support for CARMA construction was derived from the Gordon and Betty Moore Foundation, the Kenneth T. and Eileen L. Norris Foundation, the James S. McDonnell Foundation, the Associates of the California Institute of Technology, the University of Chicago, the states of California, Illinois, and Maryland, and the National Science Foundation. Ongoing CARMA development and operations are supported by the National Science Foundation under a cooperative agreement, and by the CARMA partner universities. This research has made use of the NASA/IPAC Extragalactic Database (NED) which is operated by the Jet Propulsion Laboratory, California Institute of Technology, under contract with the National Aeronautics and Space Administration. Herschel is an ESA space observatory with science instruments provided by European-led Principal Investigator consortia and with important participation from NASA. This publication makes use of data from the Galaxy Evolution Explorer, retrieved from the Mikulski Archive for Space Telescopes (MAST), part of the Space Telescope Science Institute, which is operated by the Association of Universities for Research in Astronomy, Inc., under NASA contract NAS5-26555. The Pan-STARRS1 Surveys (PS1) and the PS1 public science archive have been made possible through contributions by the Institute for Astronomy, the University of Hawaii, the Pan-STARRS Project Office, the Max-Planck Society and its participating institutes, the Max Planck Institute for Astronomy, Heidelberg and the Max Planck Institute for Extraterrestrial Physics, Garching, The Johns Hopkins University, Durham University, the University of Edinburgh, the Queen's University Belfast, the Harvard-Smithsonian Center for Astrophysics, the Las Cumbres Observatory Global Telescope Network Incorporated, the National Central University of Taiwan, the Space Telescope Science Institute, the National Aeronautics and Space Administration under grant No. NNX08AR22G issued through the Planetary Science Division of the NASA Science Mission Directorate, the National Science Foundation grant No. AST-1238877, the University of Maryland, Eotvos Lorand University (ELTE), the Los Alamos National Laboratory, and the Gordon and Betty Moore Foundation. This publication makes use of data products from the TwoMicron All Sky Survey, which is a joint project of the University of Massachusetts and the Infrared Processing and Analysis Center (IPAC)/Caltech, funded by NASA and the NSF. This publication used observations made with the Spitzer Space Telescope, which is operated by the Jet Propulsion Laboratory (JPL)/California Institute of Technology (Caltech) under a contract with NASA.

Facility: CARMA.

Appendix A
Details of Additional Photometry Measurements

We present the photometry and errors of the sources not originally in V. U et al. (2012) or J. K. Chu et al. (2017) for SED fitting in Section 3.3 in Tables 5 and 6. All UV and optical band photometry have been extinction corrected using the values of Table 7 using:

$$S_{\rm corr} = S_{\rm uncorr} * 10^{A_\lambda/2.5}$$

Appendix B
Position–Velocity Diagrams of Individual Objects

The position–velocity (PV) diagrams of each of the CARMA GOALs objects were constructed by estimating the angle across the galaxy with the largest gradient and slicing the cube at that point to create a plane. Flux perpendicular to this plane was then summed to create a PV diagram that subtended the majority of the source emission, creating an integrated intensity map across the plane slice. The PV diagrams of each CARMA GOALS source is shown in Figure A1. Double sources (i.e., sources with discrete emission) were broken out individually, including UGC 02369, CGCG 468-002, VV 250, CGCG 142-034, and NGC 6670, as shown in Figure A2. The left-hand panels for each figure show the moment0 map overlaid with the moment1 contours, as well as the chosen rotation angle for the PV slice. The right-hand panels shows the corresponding PV slice.

Table 5
Additional Photometry

Name	FUV	NUV	*g*	*r*	*i*	*J*	*H*	*K*
MCG+12-02-001	...	1.92–03	8.74–03	1.57–02	3.09–02	4.38–02	6.75–02	6.45–02
	(...)	(4.49–04)	(8.74–04)	(1.57–03)	(-9.9e+0)	(5.11–03)	(4.39–03)	(4.00–03)
UGC02608	...	...	1.13–02	1.89–02	2.26–02	5.05–02	6.51–02	5.99–02
	(...)	(...)	(1.13–03)	(1.89–03)	(−9.9e+0)	(2.49–03)	(3.21–03)	(3.39–03)
IRAS03582+6012	...	1.81–03	2.98–03	4.24–03	4.89–03	8.20–03	1.31–02	1.39–02
	(...)	(5.67–04)	(5.96–04)	(8.49–04)	(-9.9e+0)	(7.38–04)	(1.17–03)	(1.11–03)
CGCG468-002	...	9.53–04	1.29–02	2.17–02	2.79–02	6.25–02	9.13–02	8.28–02
	(...)	(2.12–04)	(1.29–03)	(2.17–03)	(-9.9e+0)	(4.04–03)	(6.35–03)	(5.91–03)
NGC2146	3.67–03	9.97–03	9.64–02	1.93–01	2.66–01	9.23–01	1.19+00	1.18+00
	(3.69–04)	(9.97–04)	(9.64–03)	(1.93–02)	(−9.9e+0)	(7.14–02)	(8.83–02)	(7.48–02)
NGC4418	...	...	1.04–02	1.83–02	2.50–02	6.10–02	6.54–02	6.13–02
	(...)	(...)	(1.04–03)	(1.83–03)	(–9.9e+0)	(3.31–03)	(4.10–03)	(5.52–03)
CGCG142-034	...	...	4.61–03	9.70–03	1.51–02	4.32–02	5.46–02	5.59–02
	(...)	(...)	(4.61–04)	(9.70–04)	(−9.9e+0)	(2.34–03)	(3.14–03)	(3.53–03)
NGC6670	2.68–04	6.03–04	5.56–03	1.05–02	1.48–02	4.32–02	5.46–02	5.59–02
	(2.72–05)	(6.04–05)	(5.56–04)	(1.05–03)	(−9.9e+0)	(2.34–03)	(3.14–03)	(3.53–03)
NGC6786	1.51–03	2.82–03	1.19–02	1.95–02	2.35–02	4.76–02	6.23–02	5.38–02
	(1.59–04)	(2.85–04)	(1.19–03)	(1.95–03)	(−9.9e+0)	(2.55–03)	(3.79–03)	(3.57–03)
NGC6926	2.90–03	5.33–03	2.97–02	4.82–02	6.05–02	1.34–01	1.56–01	1.43–01
	(2.99–04)	(5.37–04)	(2.97–03)	(4.82–03)	(−9.9e+0)	(5.67–03)	(7.56–03)	(8.18–03)
IIZw96	1.91–03	2.91–03	7.73–03	1.04–02	1.13–02	2.02–02	2.19–02	2.12–02
	(1.99–04)	(2.94–04)	(7.73–04)	(1.04–03)	(−9.9e+0)	(1.44–03)	(1.95–03)	(1.89–03)

Note. All fluxes are given in Jy, with uncertainties given on the row below.

Table 6
Additional Photometry: Spitzer

Name	IRAC1	IRAC2	IRAC3	IRAC4	MIPS1
MCG+12-02-001	5.65−02	4.85-02	1.53−01	5.39−01	4.44+00
	(1.88−03)	(1.75−03)	(6.15−03)	(2.97−02)	(3.65−01)
UGC02608	4.74−02	5.76−02	1.03−01	2.88−01	1.21+00
	(1.65−03)	(2.22−03)	(5.01−03)	(1.18−02)	(9.75−02)
IRAS03582+6012	3.81−02	6.57−02	1.84−01	2.46−01	8.19−01
	(1.19−03)	(2.08−03)	(6.07−03)	(8.41−03)	(6.55−02)
CGCG468-002	5.69−02	5.24−02	7.06−02	1.65−01	9.96−01
	(2.27−03)	(2.57−03)	(6.43−03)	(1.19−02)	(8.32−02)
NGC2146	8.62−01	6.59−01	2.45+00	7.06+00	1.70+01
	(4.14−02)	(4.59−02)	(1.92−01)	(1.44+00)	(1.38+00)
NGC4418	2.94−02	3.34−02	1.31−01	2.92−01	6.10+00
	(1.38−03)	(1.81−03)	(7.68−03)	(2.97−02)	(4.88−01)
CGCG142-034	4.04−02	3.19−02	8.28−02	3.13−01	8.59−01
	(1.37−03)	(1.23−03)	(3.33−03)	(1.04−02)	(6.92−02)
NGC6670	4.04−02	3.19−02	8.28−02	3.13−01	8.59−01
	(1.37−03)	(1.23−03)	(3.33−03)	(1.04−02)	(6.92−02)
NGC6786	3.13−02	2.22−02	4.60−02	1.63−01	4.64−01
	(1.16−03)	(1.08−03)	(2.72−03)	(6.34−03)	(3.81−02)
NGC6926	8.86−02	6.37−02	1.40−01	4.52−01	6.74−01
	(3.34−03)	(3.12−03)	(8.46−03)	(1.72−02)	(6.01−02)
IIZw96	1.76−02	1.75−02	3.70−02	1.42−01	1.90+00
	(6.17−04)	(6.58−04)	(1.58−03)	(4.78−03)	(1.52−01)

Note. All fluxes are given in Jy, with uncertainties given on the row below.

Table 7
Extinction Corrections

Name	$A_{\rm FUV}$	$A_{\rm NUV}$	A_U	A_B	A_g	A_V	A_r	A_R	A_i	A_I
MCG+12-02-001	4.564	4.762	2.669	2.233	2.034	1.689	1.407	1.336	1.046	0.927
UGC02608	1.192	1.243	0.697	0.583	0.531	0.441	0.367	0.349	0.273	0.242
IRAS03582+6012	5.307	5.538	3.104	2.597	2.366	1.964	1.637	1.554	1.216	1.078
CGCG468-002	2.610	2.724	1.527	1.277	1.164	0.966	0.805	0.764	0.598	0.530
NGC2146	0.711	0.711	0.415	0.348	0.317	0.263	0.219	0.208	0.163	0.144
NGC4418	0.173	0.173	0.101	0.085	0.077	0.064	0.053	0.051	0.040	0.035
CGCG142-034	1.013	1.057	0.593	0.497	0.452	0.375	0.313	0.297	0.233	0.206
NGC6670	0.354	0.354	0.208	0.174	0.158	0.131	0.109	0.104	0.081	0.072
NGC6786	1.048	1.094	0.614	0.513	0.468	0.388	0.324	0.307	0.240	0.213
NGC6926	1.205	1.258	0.705	0.590	0.538	0.446	0.372	0.353	0.276	0.245
IIZw96	0.619	0.619	0.362	0.303	0.276	0.229	0.191	0.181	0.142	0.126
CGCG436-030	0.270	0.270	0.158	0.132	0.120	0.100	0.083	0.079	0.062	0.055
IIIZw35	0.465	0.465	0.272	0.228	0.207	0.172	0.143	0.136	0.107	0.094
NGC695	0.667	0.667	0.390	0.326	0.297	0.247	0.206	0.195	0.153	0.135
NGC958	0.224	0.224	0.131	0.109	0.100	0.083	0.069	0.065	0.051	0.045
UGC02369	0.754	0.754	0.441	0.369	0.336	0.279	0.232	0.221	0.173	0.153
NGC1614	1.140	1.190	0.667	0.558	0.508	0.422	0.352	0.334	0.261	0.232
NGC2623	0.305	0.305	0.178	0.149	0.136	0.113	0.094	0.089	0.070	0.062
Arp55	0.127	0.127	0.075	0.062	0.057	0.047	0.039	0.037	0.029	0.026
UGC05101	0.246	0.246	0.144	0.120	0.110	0.091	0.076	0.072	0.056	0.050
Arp148	0.065	0.068	0.038	0.032	0.029	0.024	0.020	0.019	0.015	0.013
Arp299	0.124	0.124	0.072	0.060	0.055	0.046	0.038	0.036	0.028	0.025
NGC4922	0.084	0.087	0.048	0.041	0.037	0.031	0.026	0.024	0.019	0.017
IC860	0.100	0.100	0.058	0.048	0.044	0.037	0.030	0.029	0.023	0.020
VV250	0.168	0.168	0.097	0.081	0.074	0.062	0.051	0.049	0.038	0.034
NGC5256	0.097	0.10	0.057	0.047	0.043	0.036	0.030	0.028	0.022	0.020
IC5298	0.635	0.635	0.372	0.311	0.284	0.235	0.196	0.186	0.146	0.129
NGC7674	0.440	0.440	0.257	0.215	0.196	0.163	0.135	0.129	0.101	0.089

Note. Extinction corrections for the UV and optical bands used in the SED fitting. The optical extinctions are from E. F. Schlafly & D. P. Finkbeiner (2011), as given in NED. The UV extinctions are calculated from A_V based on the relations of T. K. Wyder et al. (2005).

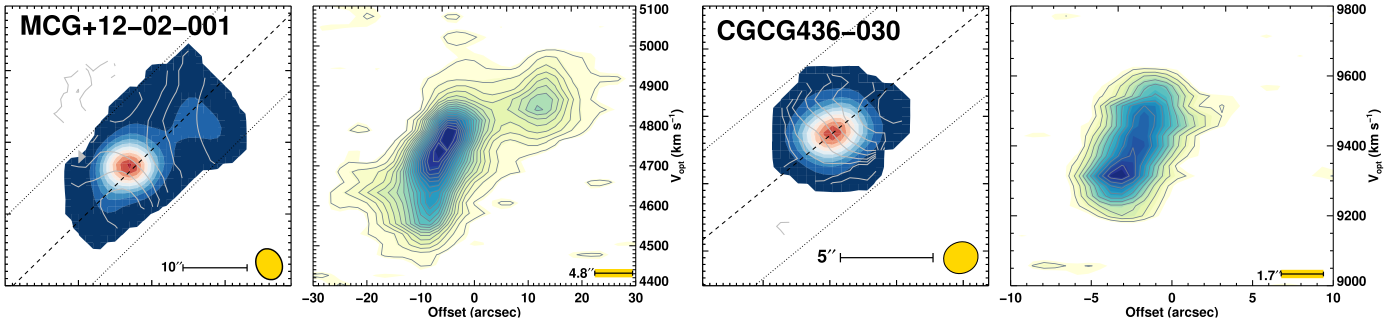

MCG+12-02-001 (left) with 5σ contour levels and CGCG 436-030 (right) with 2σ contour levels.

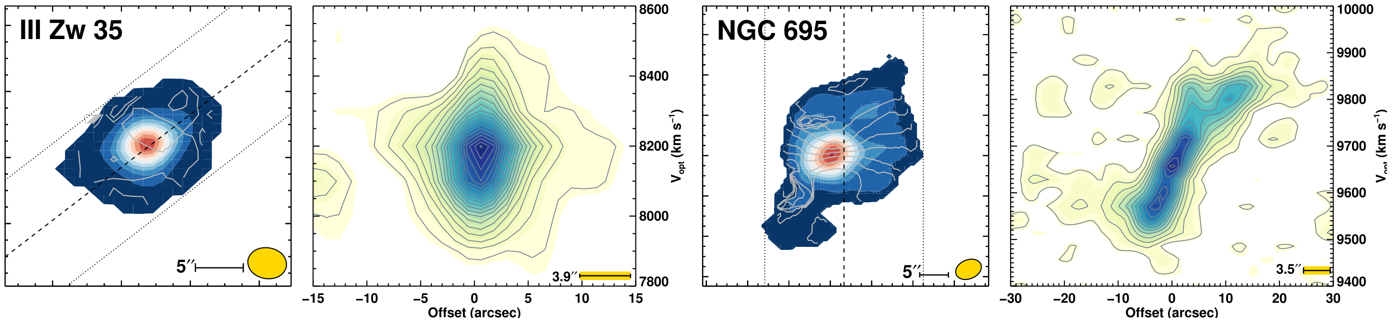

III Zw 35 (left) with 3σ contour levels and NGC 695 (right) with 6σ contour levels.

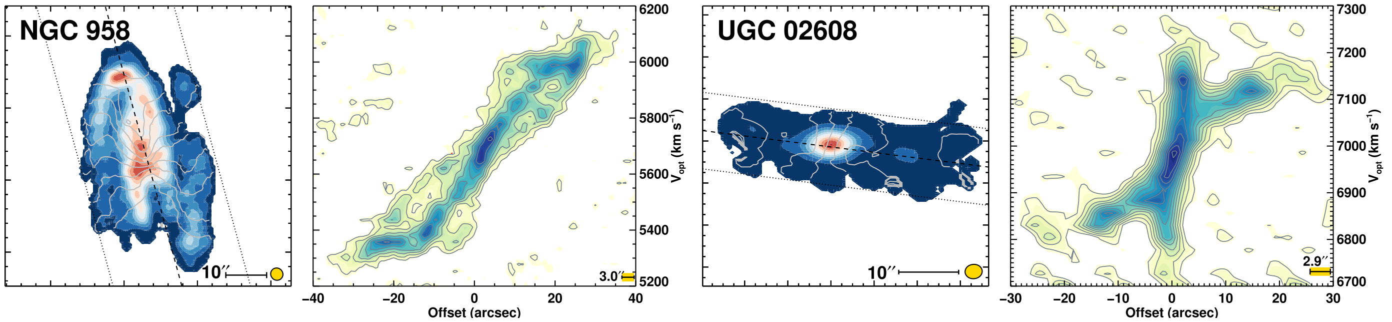

NGC 958 (left) with 4σ contour levels and UGC 02608 (right) with 4σ contour levels.

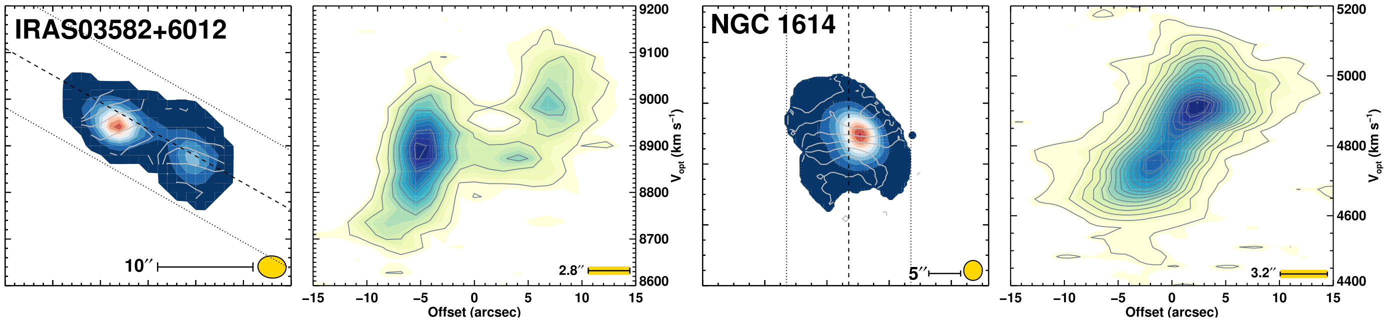

IRAS 03582+6012 (left) with 3σ contour levels and NGC 1614(right) with 8σ contour levels.

Figure A1. PV diagrams for the CARMA GOALS sample

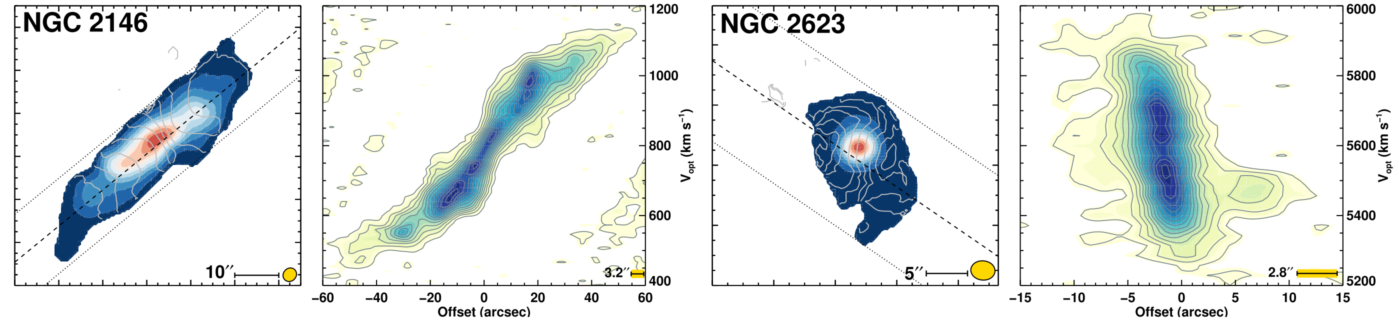

NGC 2146 (left) with 8σ contour levels and NGC 2623 (right) with 6σ contour levels.

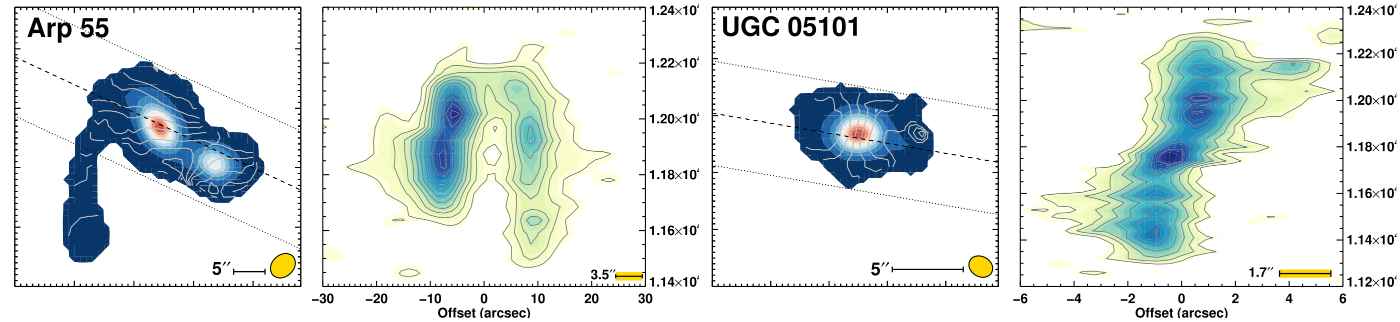

Arp 55 (left) with 4σ contour levels and UGC 05101 (right) with 3σ contour levels.

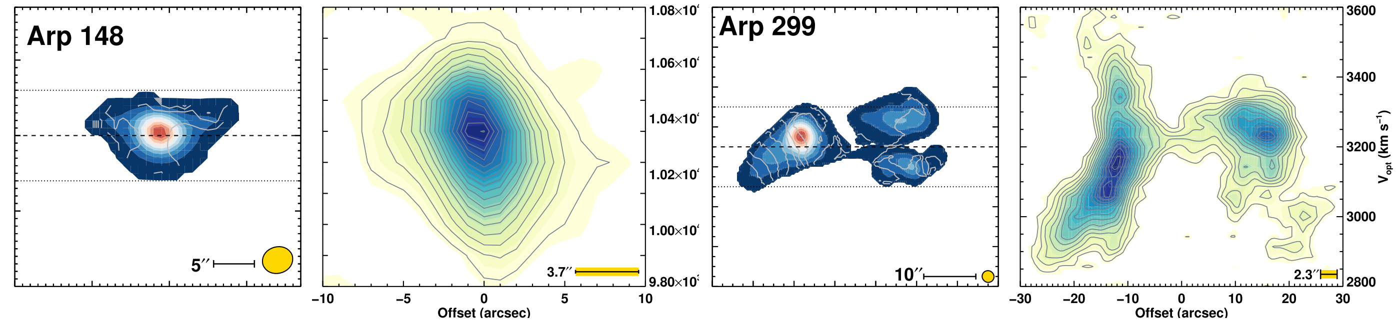

Arp 148 (left) with 3σ contour levels and 4σ contour levels.

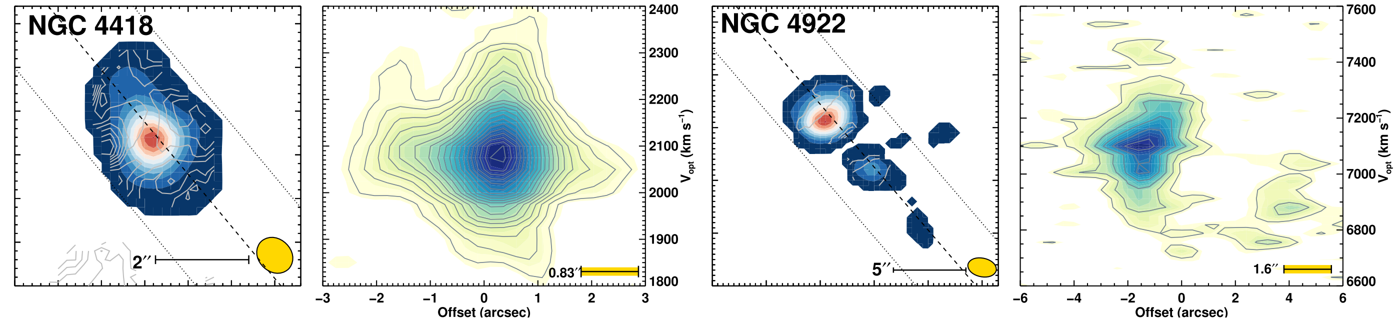

NGC 4418 (left) and NGC 4922 (right) with 3σ contour levels.

Figure A1. (Continued.)

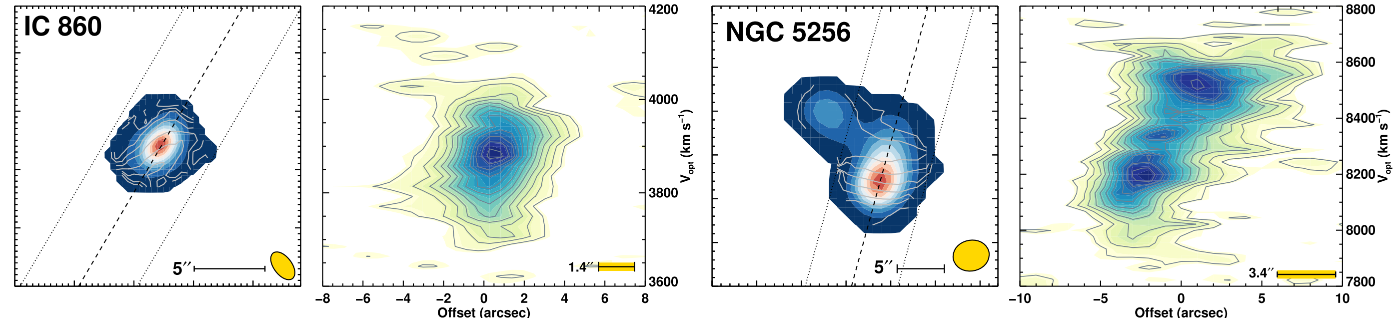

IC 860 (left) with 3σ contour levels and NGC 5256 (right) with 4σ contour levels.

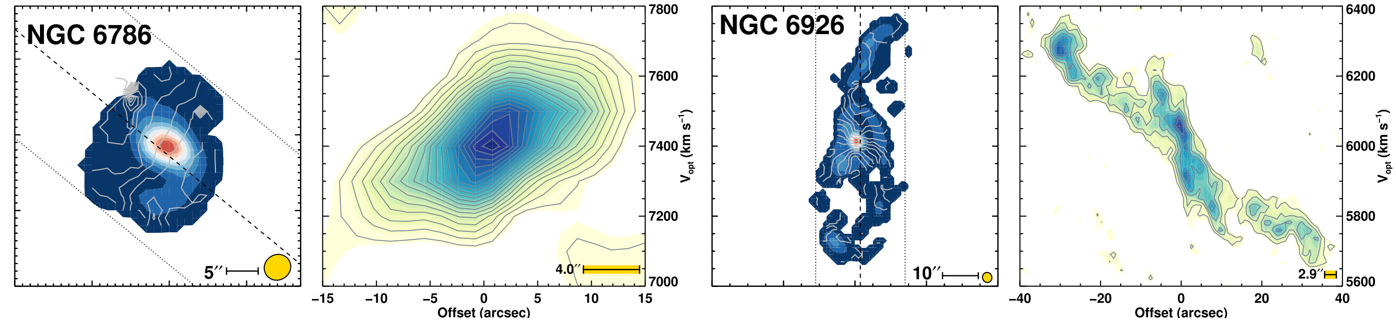

NGC 6786 (left) with 3σ contour levels and NGC 6926 (right) with 2σ contour levels.

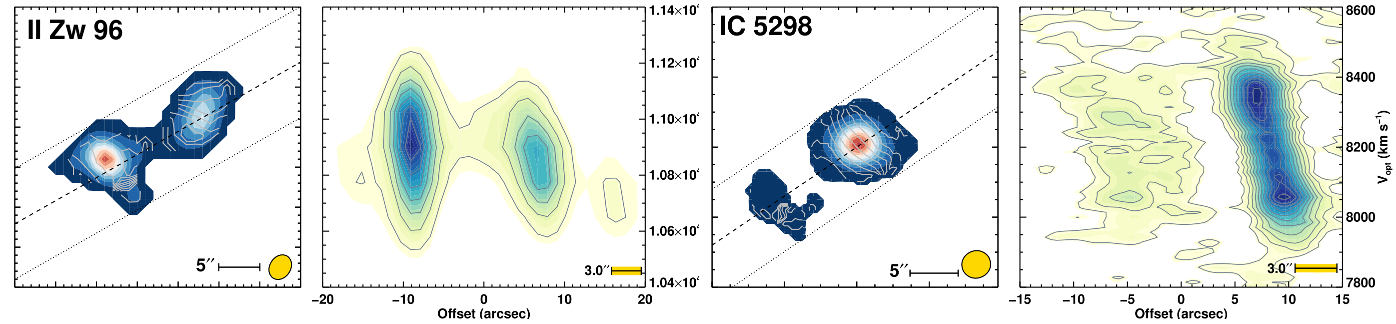

II Zw 96 (left) with 3σ contour levels and IC 5298 (right) with 6σ contour levels.

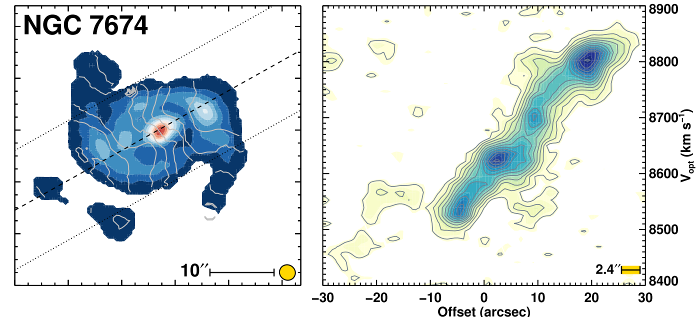

NGC 7674 with 4σ contour levels.

Figure A1. (Continued.)

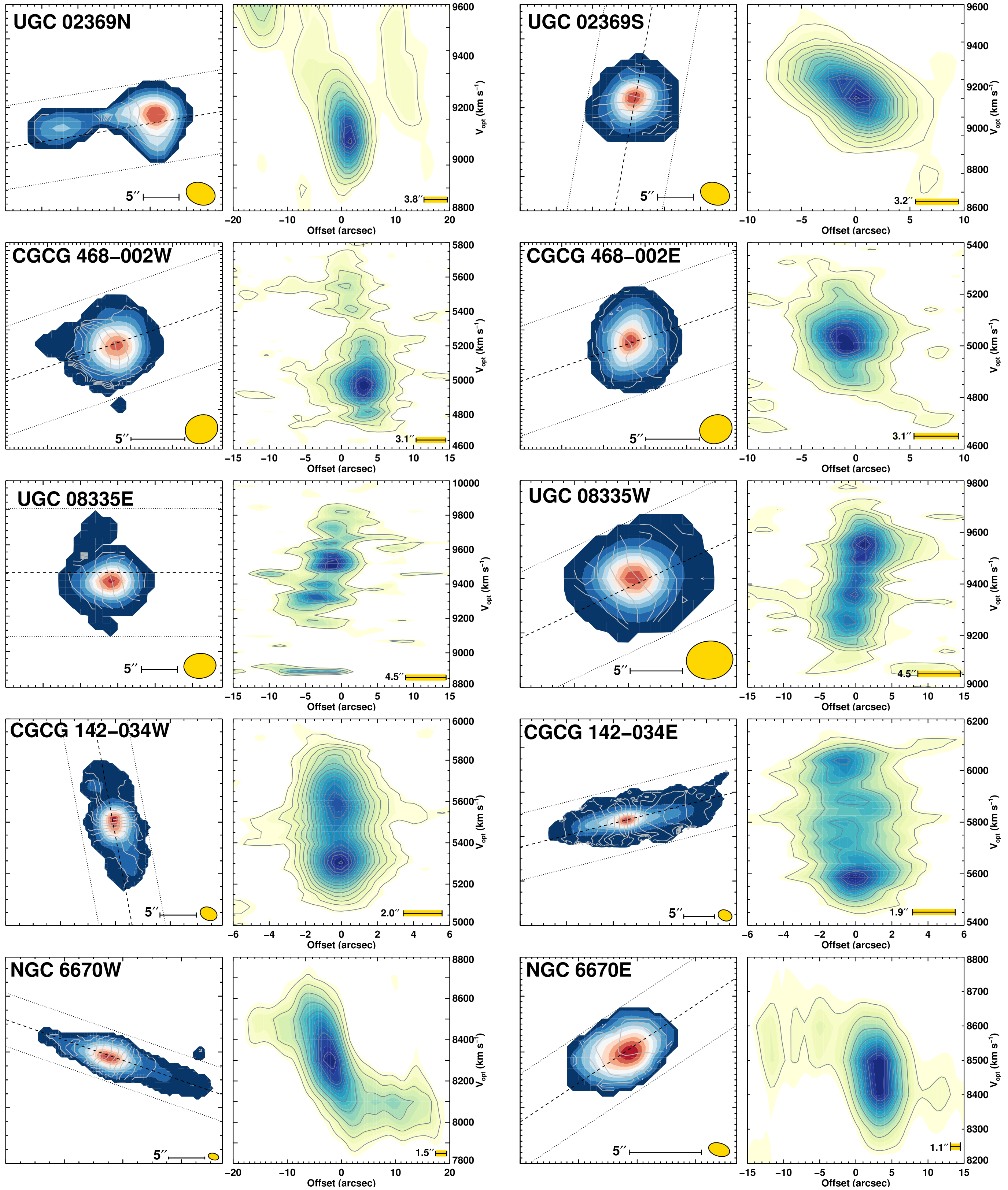

Figure A2. PV diagrams of double sources, including UGC 02369 (top row), CGCG 468-002 (second row), VV 250 (third row), CGCG 142-034 (fourth row), and NGC 6670 (bottom row). The correlator edge is seen in UGC 02369N, and it is likely that some of the flux is missing from that source.

ORCID iDs

Katherine Alatalo https://orcid.org/0000-0002-4261-2326
Andreea O. Petric https://orcid.org/0000-0003-4030-3455
Lauranne Lanz https://orcid.org/0000-0002-3249-8224
Kate Rowlands https://orcid.org/0000-0001-7883-8434
Vivian U https://orcid.org/0000-0002-1912-0024
Kirsten L. Larson https://orcid.org/0000-0003-3917-6460
Lee Armus https://orcid.org/0000-0003-3498-2973
Loreto Barcos-Muñoz https://orcid.org/0000-0003-0057-8892
Aaron S. Evans https://orcid.org/0000-0003-2638-1334
Jin Koda https://orcid.org/0000-0002-8762-7863
Yuanze Luo https://orcid.org/0000-0002-0696-6952
Anne M. Medling https://orcid.org/0000-0001-7421-2944
Kristina E. Nyland https://orcid.org/0000-0003-1991-370X
Justin A. Otter https://orcid.org/0000-0003-3191-9039
Pallavi Patil https://orcid.org/0000-0002-9471-8499
Fernando Peñaloza https://orcid.org/0000-0003-1839-5859
Diane Salim https://orcid.org/0000-0002-2858-3506
David B. Sanders https://orcid.org/0000-0002-1233-9998
Elizaveta Sazonova https://orcid.org/0000-0001-6245-5121
Maya Skarbinski https://orcid.org/0009-0004-0844-0657
Yiqing Song https://orcid.org/0000-0002-3139-3041
Ezequiel Treister https://orcid.org/0000-0001-7568-6412
C. Meg Urry https://orcid.org/0000-0002-0745-9792

References

Alatalo, K. 2015, ApJL, 801, L17
Alatalo, K., Appleton, P. N., Lisenfeld, U., et al. 2015a, ApJ, 812, 117
Alatalo, K., Crocker, A. F., Aalto, S., et al. 2015b, MNRAS, 450, 3874
Alatalo, K., Davis, T. A., Bureau, M., et al. 2013, MNRAS, 432, 1796
Alatalo, K., Lacy, M., Lanz, L., et al. 2015c, ApJ, 798, 31
Alatalo, K., Lisenfeld, U., Lanz, L., et al. 2016, ApJ, 827, 106
Alatalo, K., Nyland, K., Graves, G., et al. 2014, ApJ, 780, 186
Armus, L., Mazzarella, J. M., Evans, A. S., et al. 2009, PASP, 121, 559
Baade, W. 1958, RA, 5, 3
Baldry, I. K., Glazebrook, K., Brinkmann, J., et al. 2004, ApJ, 600, 681
Barnes, J. E., & Hernquist, L. 1992, ARA&A, 30, 705
Beaulieu, D., Petric, A., Robert, C., et al. 2023, MNRAS, 518, 1407
Berta, S., Lutz, D., Santini, P., et al. 2013, A&A, 551, A100
Bock, D. C.-J., Bolatto, A. D., Hawkins, D. W., et al. 2006, Proc. SPIE, 6267, 13
Bolatto, A. D., Wolfire, M., & Leroy, A. K. 2013, ARA&A, 51, 207
Bruzual, G., & Charlot, S. 2003, MNRAS, 344, 1000
Bryant, P. M., & Scoville, N. Z. 1999, AJ, 117, 2632
Bundy, K., Bershady, M. A., Law, D. R., et al. 2015, ApJ, 798, 7
Bustamante, S., Sparre, M., Springel, V., & Grand, R. J. J. 2018, MNRAS, 479, 3381
Calzetti, D., Kennicutt, R. C., Engelbracht, C. W., et al. 2007, ApJ, 666, 870
Canalizo, G., & Stockton, A. 2000, AJ, 120, 1750
Center, G. S. F. 2004, GALEX Observer's Guide.Goddard Space Flight Center, Greenbelt, MD, 619, L1, https://asd.gsfc.nasa.gov/archive/galex/FAQ/countsbackground.html
Chabrier, G. 2003, PASP, 115, 763
Chambers, K. C., Magnier, E. A., Metcalfe, N., et al. 2016, arXiv:1612.05560
Charlot, S., & Fall, S. M. 2000, ApJ, 539, 718
Chu, J. K., Sanders, D. B., Larson, K. L., et al. 2017, ApJS, 229, 25
Cicone, C., Maiolino, R., Sturm, E., et al. 2014, A&A, 562, A21
Cohen, M., Megeath, S. T., Hammersley, P. L., Martín-Luis, F., & Stauffer, J. 2003, AJ, 125, 2645
Combes, F., García-Burillo, S., Braine, J., et al. 2013, A&A, 550, A41
Costagliola, F., Aalto, S., Sakamoto, K., et al. 2013, A&A, 556, A66
Cutri, R., Skrutskie, M., Van Dyk, S., et al. 2006, Explanatory Supplement to the 2MASS All Sky Data Release and Extended Mission Products.IPAC, Pasadena, CA, http://www.ipac.caltech.edu/2mass/releases/allsky/doc/explsup.html
da Cunha, E., Charlot, S., & Elbaz, D. 2008, MNRAS, 388, 1595
Davis, T. A., Young, L. M., Crocker, A. F., et al. 2014, MNRAS, 444, 3427
Di Matteo, T., Springel, V., & Hernquist, L. 2005, Natur, 433, 604
Díaz-Santos, T., Charmandaris, V., Armus, L., et al. 2011, ApJ, 741, 32
Downes, D., & Solomon, P. M. 1998, ApJ, 507, 615
Engelbracht, C. W., Blaylock, M., Su, K. Y. L., et al. 2007, PASP, 119, 994
Faber, S. M., Willmer, C. N. A., Wolf, C., et al. 2007, ApJ, 665, 265
Falstad, N., Aalto, S., König, S., et al. 2021, A&A, 649, A105
Fazio, G. G., Hora, J. L., Allen, L. E., et al. 2004, ApJS, 154, 10
Federrath, C. 2013, MNRAS, 436, 3167
Feltre, A., Hatziminaoglou, E., Fritz, J., & Franceschini, A. 2012, MNRAS, 426, 120
Fensch, J., & Bournaud, F. 2021, MNRAS, 505, 3579
Feruglio, C., Maiolino, R., Piconcelli, E., et al. 2010, A&A, 518, L155
Fisher, D. B., Bolatto, A., Drory, N., et al. 2013, ApJ, 764, 174
Fitzpatrick, E. L. 1999, PASP, 111, 63
French, K. D., Yang, Y., Zabludoff, A., et al. 2015, ApJ, 801, 1
Fritz, J., Franceschini, A., & Hatziminaoglou, E. 2006, MNRAS, 366, 767
Gao, Y., & Solomon, P. M. 2004, ApJ, 606, 271
García-Burillo, S., Combes, F., Usero, A., et al. 2014, A&A, 567, A125
García-Burillo, S., Combes, F., Usero, A., et al. 2015, A&A, 580, A35
Genzel, R., Price, S. H., Übler, H., et al. 2020, ApJ, 902, 98
Genzel, R., Tacconi, L. J., Gracia-Carpio, J., et al. 2010, MNRAS, 407, 2091
González-Alfonso, E., Fischer, J., Sturm, E., et al. 2015, ApJ, 800, 69
Guillard, P., Boulanger, F., Lehnert, M. D., et al. 2015, A&A, 574, A32
Harrison, C. M., Alexander, D. M., Mullaney, J. R., & Swinbank, A. M. 2014, MNRAS, 441, 3306
He, H., Bottrell, C., Wilson, C., et al. 2023, ApJ, 950, 56
Herrero-Illana, R., Privon, G. C., Evans, A. S., et al. 2019, A&A, 628, A71
Holmberg, E. 1941, ApJ, 94, 385
Hopkins, P. F., Hernquist, L., Cox, T. J., & Kereš, D. 2008, ApJS, 175, 356
Howell, J. H., Armus, L., Mazzarella, J. M., et al. 2010, ApJ, 715, 572
Hubble, E. P. 1926, ApJ, 64, 321
Hubble, E. P. 1936, Realm of the Nebulae (Yale University Press)
Iono, D., Yun, M. S., & Mihos, J. C. 2004, ApJ, 616, 199
Kawamuro, T., Ricci, C., Imanishi, M., et al. 2022, ApJ, 938, 87
Kennicutt, R. C., Jr. 1998, ApJ, 498, 541
König, S., Aalto, S., Muller, S., et al. 2016, A&A, 594, A70
Kormendy, J., & Ho, L. C. 2013, ARA&A, 51, 511
Krumholz, M. R., Dekel, A., & McKee, C. F. 2012, ApJ, 745, 69
Lacy, M., Baum, S. A., Chandler, C. J., et al. 2020, PASP, 132, 035001
Lacy, M., Petric, A. O., Sajina, A., et al. 2007, AJ, 133, 186
Lacy, M., Ridgway, S. E., Gates, E. L., et al. 2013, ApJS, 208, 24
Lanz, L., Hayward, C. C., Zezas, A., et al. 2014, ApJ, 785, 39
Lanz, L., Ogle, P. M., Alatalo, K., & Appleton, P. N. 2016, ApJ, 826, 29
Larson, K. L., Sanders, D. B., Barnes, J. E., et al. 2016, ApJ, 825, 128
Lu, N., Zhao, Y., Xu, C. K., et al. 2014, ApJL, 787, L23
Luo, Y., Rowlands, K., Alatalo, K., et al. 2022, ApJ, 938, 63
Lutz, D., Sturm, E., Janssen, A., et al. 2020, A&A, 633, A134
Manohar, S., & Scoville, N. 2017, ApJ, 835, 127
Martin, D. C., Fanson, J., Schiminovich, D., et al. 2005, ApJL, 619, L1
Mihos, J. C., & Hernquist, L. 1996, ApJ, 464, 641
Murphy, E. J., Bremseth, J., Mason, B. S., et al. 2012, ApJ, 761, 97
Ogle, P., Boulanger, F., Guillard, P., et al. 2010, ApJ, 724, 1193
Oke, J. B., & Gunn, J. E. 1983, ApJ, 266, 713
Pan, H.-A., Lin, L., Hsieh, B.-C., et al. 2018, ApJ, 868, 132
Petric, A. O., Armus, L., Flagey, N., et al. 2018, AJ, 156, 295
Petric, A. O., Armus, L., Howell, J., et al. 2011, ApJ, 730, 28
Pilbratt, G. L., Riedinger, J. R., Passvogel, T., et al. 2010, A&A, 518, L1
Quintero, A. D., Hogg, D. W., Blanton, M. R., et al. 2004, ApJ, 602, 190
Renaud, F., Bournaud, F., Daddi, E., et al. 2019, A&A, 621, A104
Renaud, F., Bournaud, F., Kraljic, K., & Duc, P.-A. 2014, MNRAS, 442, L33
Ricci, C., Chang, C.-S., Kawamuro, T., et al. 2023, ApJL, 952, L28
Ricci, C., Trakhtenbrot, B., Koss, M. J., et al. 2017, ApJS, 233, 17
Rich, J. A., Kewley, L. J., & Dopita, M. A. 2011, ApJ, 734, 87
Rieke, G. H., Young, E. T., Engelbracht, C. W., et al. 2004, ApJS, 154, 25
Rowlands, K., Dunne, L., Maddox, S., et al. 2012, MNRAS, 419, 2545
Rowlands, K., Wild, V., Nesvadba, N., et al. 2015, MNRAS, 448, 258
Saade, M. L., Brightman, M., Stern, D., et al. 2022, ApJ, 936, 162
Sakamoto, K., Aalto, S., Combes, F., Evans, A., & Peck, A. 2014, ApJ, 797, 90
Sakamoto, K., Aalto, S., Costagliola, F., et al. 2013, ApJ, 764, 42
Salim, D. M., Alatalo, K., Federrath, C., Groves, B., & Kewley, L. J. 2020, ApJ, 893, 26
Salim, D. M., Federrath, C., & Kewley, L. J. 2015, ApJL, 806, L36
Sanders, D. B., Mazzarella, J. M., Kim, D.-C., Surace, J. A., & Soifer, B. T. 2003, AJ, 126, 1607
Sandstrom, K. M., Leroy, A. K., Walter, F., et al. 2013, ApJ, 777, 5
Sault, R. J., Teuben, P. J., & Wright, M. C. H. 1995, in ASP Conf. Ser.Vol. 77, Astronomical Data Analysis Software and Systems IV, ed. R. A. Shaw,

H. E. Payne, & J. J. E. Hayes (San Francisco, CA: ASP), 433, arXiv:astro-ph/0612759
Schlafly, E. F., & Finkbeiner, D. P. 2011, ApJ, 737, 103
Schmidt, M. 1959, ApJ, 129, 243
Skrutskie, M. F., Cutri, R. M., Stiening, R., et al. 2006, AJ, 131, 1163
Sparre, M., & Springel, V. 2016, MNRAS, 462, 2418
Spergel, D. N., Bean, R., Doré, O., et al. 2007, ApJS, 170, 377
Stanley, F., Jones, B. M., Riechers, D. A., et al. 2023, ApJ, 945, 24
Stern, D., Assef, R. J., Benford, D. J., et al. 2012, ApJ, 753, 30
Stern, D., Eisenhardt, P., Gorjian, V., et al. 2005, ApJ, 631, 163
Stierwalt, S., Armus, L., Charmandaris, V., et al. 2014, ApJ, 790, 124
Strateva, I., Ivezić, Ž., Knapp, G. R., et al. 2001, AJ, 122, 1861
Teyssier, R., Chapon, D., & Bournaud, F. 2010, ApJL, 720, L149
Thorp, M. D., Ellison, S. L., Pan, H.-A., et al. 2022, MNRAS, 516, 1462
Tinsley, B. M. 1978, ApJ, 222, 14
Toomre, A., & Toomre, J. 1972, ApJ, 178, 623
U, V., Sanders, D. B., Mazzarella, J. M., et al. 2012, ApJS, 203, 9
Ueda, J., Iono, D., Yun, M. S., et al. 2014, ApJS, 214, 1
Vavilkin, T. 2011, PhD thesis, Department of Physics & Astronomy, Stony Brook Univ., Stony Brook, NY 11794-3800, USA
Werner, M. W., Roellig, T. L., Low, F. J., et al. 2004, ApJS, 154, 1
Wyder, T. K., Treyer, M. A., Milliard, B., et al. 2005, ApJL, 619, L15
Yamashita, T., Komugi, S., Matsuhara, H., et al. 2017, ApJ, 844, 96
Zabludoff, A. I., Zaritsky, D., Lin, H., et al. 1996, ApJ, 466, 104